# Investigating the Effect on a Metal Pincer Complex when Fluorine, Carbon and Silicon based Electrophiles are Introduced into the Ligand Backbone

Daniel Picthall

MSc by Research

University of York
Chemistry

December 2020

# Abstract

This thesis describes introducing F-, C- and Si-based groups into the backbone of a pincer ligand and studying what effect this has on the geometry and onward reactivity on the metal pincer complex. The groups chosen were F, $CF_3$, $CH_3$, $SiH_3$, $^t$Bu and trimehtylsilane (TMS). Attempts to synthesise the F- and $CF_3$- substituted ruthenium pincer complexes were unsuccessful due to protonation of the dearomatized intermediate pincer complex. However, NMR and ESI-MS data did show evidence of the desired products as a result of F and $CF_3$ addition, but these products could not be isolated. This shows an alternative method to synthesising asymmetric pincer complexes is possible. Alkylating agents were also used however unfortunately similar results were obtained. Geometry optimisations of the substituted metal pincer complexes (metals studied = Ru, Fe and Mg) using DFT theory showed that the introduction of these groups has a minor influence on the structure of the complex. However, on changing the nature of the metal centre to a group II metal (magnesium), significant distortion of the complex is observed. Computational calculations investigating proton transfer to the dearomatized complex with a substituent in the ligand backbone showed that by changing the nature of the group from electron-withdrawing ($CF_3$) to electron-donating ($^t$Bu), proton transfer to the dearomatized complex became more facile. This study showed that by introducing substituents into the ligand backbone the reactivity of a pincer complex can be manipulated

# Table of Contents

# List of Figures

# List of Schemes

# List of Tables

# Acknowledgements

Firstly, I would like to thank my supervisors, Jason and John, for their constant support and advice throughout my time at the University of York. I would also like to thank Heather Fish for support with the NMR facilities and Karl Heaton for providing all mass spectrometry data. I'd like to thank the wider JMS/JML group for their guidance throughout the year and making the lab a friendly place to work. Finally, I would like to thank my mam for her constant support and encouragement.

# Author Declaration

I declare that this thesis is presentation of original work and I am the sole author. This work has not been previously presented for an award at this, or any other, University. All sources are acknowledged as references.

# 1.Introduction

## 1.1 Formation of C-F Bonds

The selective fluorination of C-H bonds is a transformation that has been heavily studied owing in part to the various properties fluorine can impart on a molecule, many of which are of particular interest to both the pharmaceutical and agrochemical industries. However, the selective formation of C-F bonds presents a significant synthetic challenge due to the properties possessed by fluorine and the experimental conditions required such as high temperatures and reagents that have been shown to be difficult to handle. The discovery of catalytic methodologies for the mild and selective formation of C-F bonds along with the development of mild fluorinating agents (nucleophilic and electrophilic) led to an increased interest in the field and significant advances have been made over the last 20 years. This section will describe briefly previous reported methods for C-F bond formation mediated by transition metals. The examples given will show how problems previously encountered with C-F bond formation such as selectivity have been overcome and how these methods have evolved over time. The synthetic methods that are focused on are those using nucleophilic and electrophilic fluorine sources. A novel fluorination mechanism, outer-sphere electrophilic fluorination (OSEF) will also be outlined. OSEF is of particular importance to this project as this work aims to demonstrate the ability to directly form a new C-F bond in the backbone of a pincer ligand, building on previous work carried out with the OSEF mechanism.

### 1.1.1 Nucleophilic Transition Metal Mediated Fluorination

In nucleophilic fluorination reactions alkali-metal salts, such as potassium fluoride (KF) and silver fluoride (AgF), are often employed as sources of fluorine. However, nucleophilic fluorination presents several challenges that must be overcome to achieve selective fluorination in a reasonable yield. Examples of these include the high basicity of the fluoride anion which can lead to unwanted side reactions, the requirement for aprotic solvents to ensure the nucleophilicity of $F^-$ is not hindered by hydrogen-bond interactions and also the alkali-metal salts used as fluoride sources suffer from poor solubility and so additives such as crown ethers are required to improve solubility.[1] Despite the significant challenges presented in nucleophilic fluorination synthetic routes to allylic fluorides, aryl fluorides and fluorohydrins have been developed.[2–6]

The synthesis of aryl fluorides is an important transformation, due to their importance in the pharmaceutical industry. Although work had been carried out using electrophilic fluorine sources to form aryl fluorides, up until 2009 no method existed for transition metal-catalysed aryl fluorination.[7] Buchwald *et al.* were the first to outline the catalytic formation of aryl fluorides using a nucleophilic fluorine source. Their paper describes the conversion of aryl triflates to the corresponding aryl fluoride via reductive elimination from a Pd(II) complex.[4] Catalytic cycles involving reductive elimination to form Ar-F have proven difficult to design, due to the high barrier for formation of Ar-F from a $Pd^{II}$-F intermediate and also due to the basicity of the fluoride anion, side reactions are often seen involving the supporting ligands. To overcome this Buchwald *et al*. used a monophosphine ligand, ${}^{t}$BuBrettPhos (Figure 1.1), as this had been shown to aid reductive elimination in previous work carried out by the same group investigating aryl aminations.[4] This ligand helps to stabilise the intermediate aryl-$Pd^{II}$-F species.

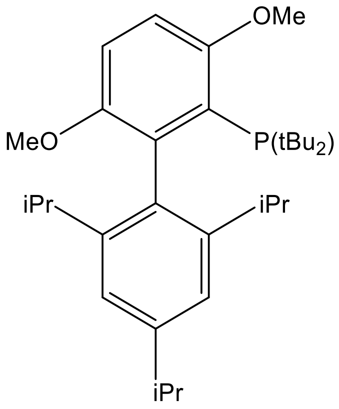

**Figure 1.1.** $^{t}$BuBrettPhos supporting ligand.

In test reactions where this supporting ligand was employed, the yield of fluorinated product increased from 30% to 79% using CsF as the fluoride source and a palladium catalyst as shown in scheme 1.1.

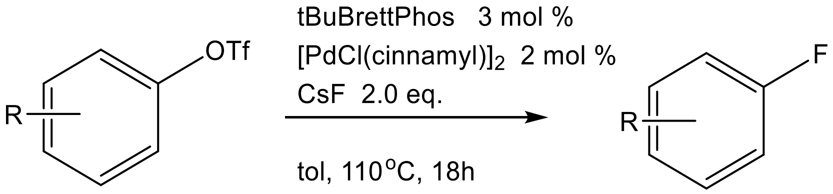

**Scheme 1.1** Reaction scheme for fluorination of aryl triflates.

These conditions gave substantial substrate scope with both hindered and electron-deficient aryl triflates being successfully converted to the corresponding aryl fluorides. Ribas *et al*. had previously demonstrated halide exchange mediated by a $Cu^{I}/Cu^{III}$ catalytic cycle and following on from Buchwald's work showing that Ar-F formation is possible via reductive elimination, Ribas and his group looked to extend their halide exchange mechanism to fluorine.[3] Initially they carried out a stoichiometric reaction with Aryl-$Cu^{III}$-Cl and AgF to determine if the desired fluorinated product could be formed. This reaction yielded the aryl-fluoride product in up to 90% yield. Given the relative success of this reaction the catalytic fluoride insertion into the structure shown in figure 1.2 using AgF was investigated.

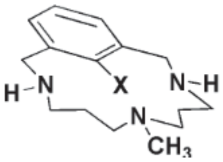

**Figure 1.2** Structure used for halide exchange**.**

Catalytic fluoride insertion at first was difficult as the yields of fluorinated product obtained were around 40%, with the main by-product of the reaction being due to intramolecular aryl-amine coupling. This suggested decomposition of the aryl-Cu$^{III}$-X intermediate species. However, with slow addition of AgF the yield of the fluorinated product was now 76% with 20% yield of coupling side product. The formation of the coupling side product was believed to be due to deprotonation of the secondary amines present in the structure shown in figure 1.2. To prevent deprotonation of these amine sites and instead promote halide exchange with fluoride, methyl substituted amines were used and in doing this quantitative yield of the fluorinated product was obtained (Scheme 1.2).[3]

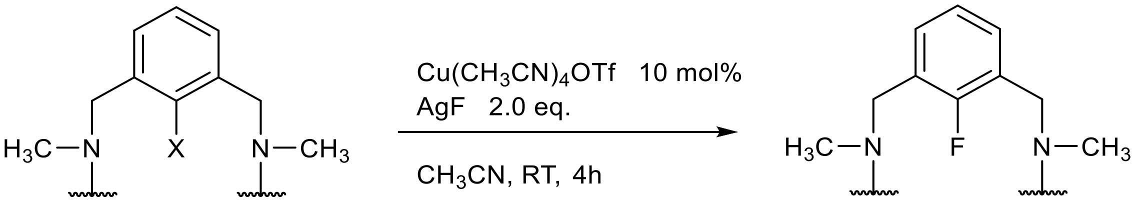

**Scheme 1.2** Reaction scheme showing formation of aryl fluoride via Cu$^{I}$/Cu$^{III}$ catalytic cycle.

Whilst the formation of aryl-fluoride bonds had been heavily investigated, one area that had so far received little attention was the formation of aliphatic C-F bonds. One of the early papers describing aliphatic C-F formation was by *Doyle and Katcher* in 2010 which described the enantioselective formation of allylic fluorides using a palladium catalyst.[5] Initially in their experiments a $Pd^{II}$ allyl intermediate was reacted with sources of $F^-$ to determine the feasibility of this reaction. When CsF and KF were used a diene side product was the dominant product, owing to the high basicity of the fluoride. However, when less basic fluoride sources were used such as AgF the allylic fluoride product was obtained with minimal side product formation. Having shown that this reaction was viable a catalytic method was then developed. The catalytic reaction for the desired allylic fluoride product can be seen in scheme 1.3.

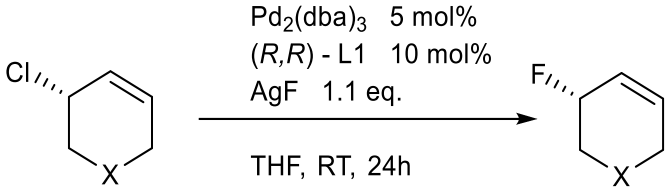

**Scheme 1.3** Catalytic synthesis of allylic fluoride.

In this reaction the Pd(0) catalyst and substrate combine to form an intermediate analogous to the one used in the reaction described in scheme 1.2. A hypothesis proposed in this paper was that from this intermediate AgCl is eliminated which helps to drive the formation of the new C-F bond.[5] Investigations into the scope of this reaction showed that it tolerated a wide range of functional groups particularly fluoride-sensitive functional groups such as silyl ethers and alcohols. Both functional groups gave good yield of desired product and showed good enantioselectivity with yields >80% and ee values again >80%. This work was then extended by the same group however acyclic allylic halides were investigated to determine if they underwent fluorination.[8] The purpose of this research was to extend the work carried out previously to acyclic substrates. In a test reaction a simple acyclic chloride was used in the presence of AgF and $PPh_3$ as a supporting ligand. The desired fluorination product was observed and the presence of $PPh_3$ increased the regioselectivity with a

6:1 ratio of branched:linear product.

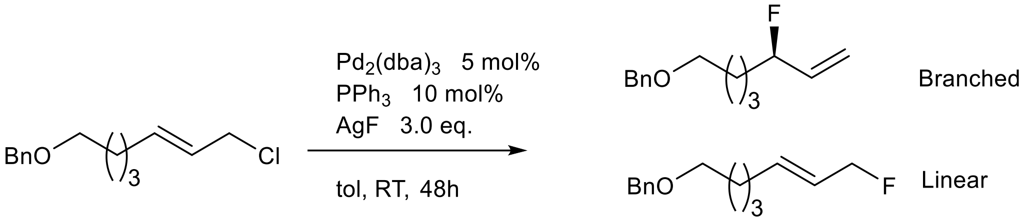

**Scheme 1.4** Fluorination of allylic halides.

Although the use of PPh3 allowed for selectivity toward the branched configuration improvements could still be made. To improve the regioselectivity of the reaction further bidentate phosphine ligands bearing large bite angles were investigated as it had been shown that as the bite angle increased the regioselectivity of the reaction also increased. A variation of the Trost ligand shown in figure 1.3 was used in the fluorination of cyclic allylic fluorides as this gave high regioselectivity with a product ratio of 20:1 (branched: linear).

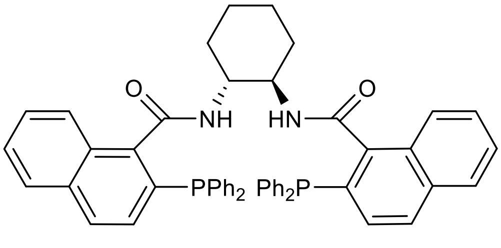

**Figure 1.3** Supporting ligand used in fluorination of acyclic allylic halides**.**

Although the ability to achieve high regioselectivity with this reaction had been demonstrated the enantioselectivity of the reaction was still low compared to the values achieved with cyclic substrates.[5,8] To increase the ee of these reactions $\alpha$-

branched allylic chlorides and those bearing heteroatom substituents were used. By introducing substituents with greater electronic and steric influence the enantioselectivity of the reaction increased with >90% ee being achieved with each reaction. This method shows a synthetic route to form an aliphatic C-F bond with both high regio- and enantioselectivity.

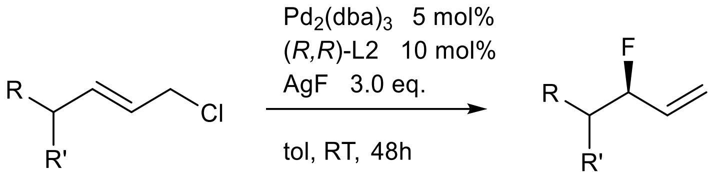

**Scheme 1.5** Selective fluorination of allylic chloride.

## 1.1.2 Transition Metal-Mediated Electrophilic Fluorination.

For many years the formation of C-F bonds using an electrophilic fluorine source was a difficult transformation to achieve, as reagents such as hypofluorites and $XeF_2$ were needed. These are difficult to use due to high reactivity and tolerance toward sensitive functional groups.[1] However, electrophilic fluorination underwent a renaissance with the introduction of mild, bench-stable reagents such as *N*-fluorobis(phenyl)sulfonimide (NFSI), Selectfluor and 2,4,6-trimethylpyridinium tetrafluoroborate (FTMP). These reagents allowed for transition metal catalysed electrophilic fluorination reactions to be carried out under mild conditions, which allows for a large substrate scope as a wider range of functional groups can be tolerated and also with good selectivity.[1,7,17,18,9–16]

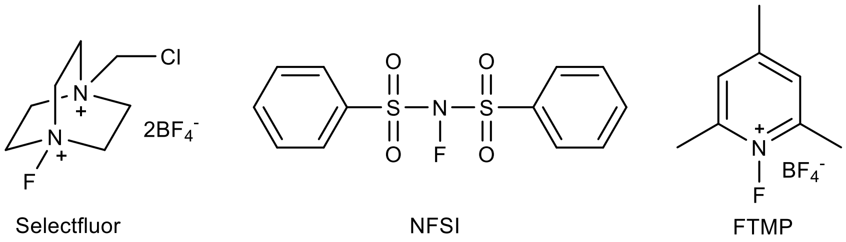

**Figure 1.4** Electrophilic fluorinating reagents.

The first example of a palladium-catalysed C-F bond formation was reported by *Sanford et al.* in 2006.[7] This paper described the fluorination of 8-methylquinoline, which was selected as it had been used in previous research into palladium catalysed C-H activation, the palladium catalyst used was $Pd(OAc)_2$. The mechanism proposed in this paper for the fluorination of 8-methylquinoline follows the same route as for the nucleophilic reactions described above with a $Pd^{II}$ intermediate formed, followed by reductive elimination of the fluorinated species.[7]

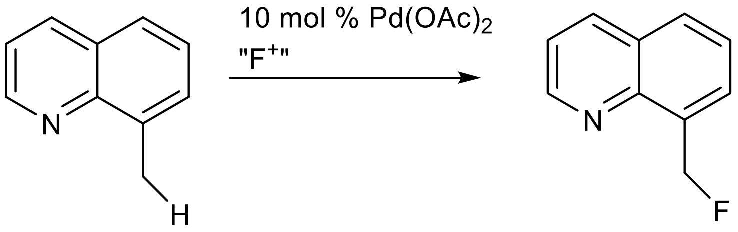

**Scheme 1.6** Palladium catalysed fluorination of 8-methylquinoline.

Various electrophilic fluorine sources were investigated for the reaction shown in scheme 1.6 such as NFSI, FTMP and selectfluor (figure 1.4). Modest yields of the fluorinated product were obtained with FTMP giving the greatest yield of 36%. This yield was dramatically increased with the addition of microwave heating with FTMP now giving a yield of 75%. This work was built upon by Yu *et al.* in 2009 who demonstrated the $Pd(OTf)_2.2H_2O$ catalysed formation of on aryl-F bond without the need for microwave irradiation. Although no microwave irradiation was required, *N*-

methylpyrrolidinone (NMP) was required to obtain reasonable yields of the desired fluorinated product.[9]

**Scheme 1.7** Ortho-fluorination of a benzylamine.

The reaction shown in scheme 1.7 gave the desired fluorinated product in yields of up to 88% however if NMP was not added to the reaction then the yield decreased significantly to approximately 5%. A range of electron withdrawing and donating substituents were tested in this scheme and all gave the monofluorinated product in varying yields.

Although palladium-based catalysts have received much attention, other transition metals have shown ability to mediate/catalyse the formation of C-F bonds, an example of this is copper.[12–14] The selective fluorination of adamantane has been demonstrated utilising a copper bis(imine) catalyst, other additives were used to aid fluorination which can be seen in scheme 1.8.[13]

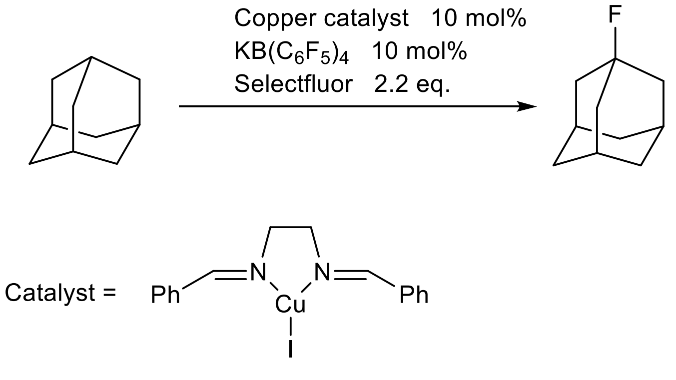

**Scheme 1.8** Fluorination of adamantane.

Initially the reaction shown in scheme 1.8 was carried out using the copper iodide salt and selectfluor. While this reaction did form the fluorinated adamantane species no appreciable yield of the product was obtained. To increase the yield of the fluorinated product $KB(C_6F_5)_4$ was added to enhance solubility and the bis(imine) ligand shown in scheme 1.8 was introduced to improve the efficiency of the metal catalyst. With the addition of the ligand and $KB(C_6F_5)_4$ the yield of the desired fluorinated product increased from 18% to 75% showing a dramatic increase. Although the adamantane reaction showed success attempts to extend the scope of this reaction to aliphatic and benzylic substrates were unsuccessful with only trace amounts of the fluorinated products detected.[13] Another example of a copper catalyst being employed in electrophilic fluorination is in the fluorination of aryl stannanes and aryl trifluoroborates.[12] A paper by Sanford *et al.* in 2013 showed how aryl fluorides could be formed from the corresponding stannane and borane analogues under mild conditions. In this work $(^tBuCN)_2CuOTf$ was employed as a catalyst alongside FTMP as the fluorine source. A combination of an aryl stannane, the copper catalyst and FTMP formed the aryl fluoride in a low yield of 6% with the major by-product in the reaction due to coupling of the aryl stannane. To prevent this and to push fluorination, FTMP was added to the copper catalyst to oxidise it followed by addition of the stannane, this intermediate then reductively eliminates the aryl fluoride. This step-by-step process increased the yield to 74%.

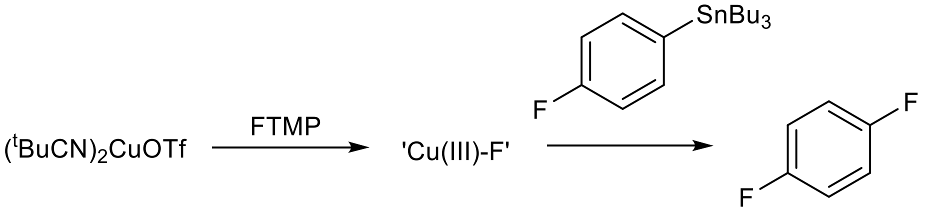

**Scheme 1.9** Scheme showing the fluorination of an aryl stannane.

After showing that aryl stannanes could be used to afford aryl fluorides, aryl boron species were then investigated. The same approach as for aryl stannanes was employed (scheme 1.9). The boron species gave low yields between 1 and 7% with the greatest yield obtained when trifluoroborate was used as a reagent however the yields were improved to approximately 60% when MeCN was used as a solvent in place of EtOAc.[12]

## 1.1.3 Outer-Sphere Electrophilic Fluorination

While the methods described in the previous sections show success in the selective formation of C-F bonds, transition metal-mediated fluorination reactions still present various challenges. Nucleophilic fluorination reactions, for example, suffer from the basicity of $F^-$ which can result in the formation of side products. In electrophilic reactions directing groups and pre-activated substrates are required to form the fluorinated product with any degree of selectivity and in reasonable yields. In 2015 a paper described a novel fluorination mechanism, outer-sphere electrophilic fluorination (OSEF), which required no functionalisation of substrates or additives.[19] The reaction described in this paper shows the selective alkyl fluorination of a vinyl group and importantly the fluorinated species is retained within the coordination sphere of the metal allowing for its further reactivity to be studied as shown in scheme 1.10.

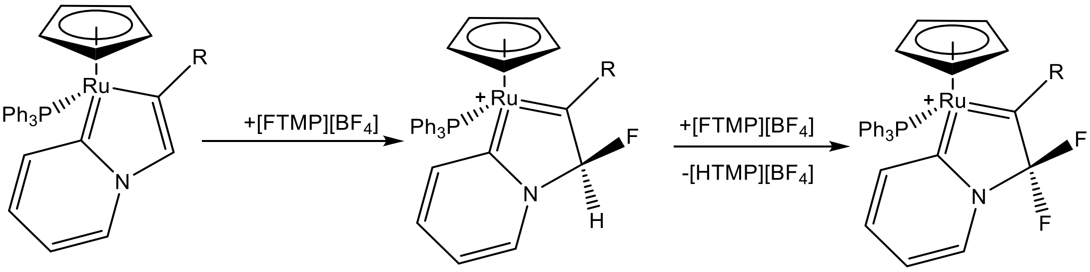

**Scheme 1.10** Formation of C-F bond and onward reactivity.

Mechanistic investigations via NMR spectroscopy showed no evidence of an intermediate species like in previous transition metal mediated fluorination reactions (M-F species) suggesting that the fluorine directly attaches to the fluorinated position. OSEF has also been used to allow the synthesis and characterisation of highly reactive compounds.[20] In this reaction a metal alkynyl complex was fluorinated to form the intermediate cationic vinylidene complex which was then deprotonated to yield the desired fluoroalkyne. The fluoroalkyne was found to be stable over an extended period of time.[20]

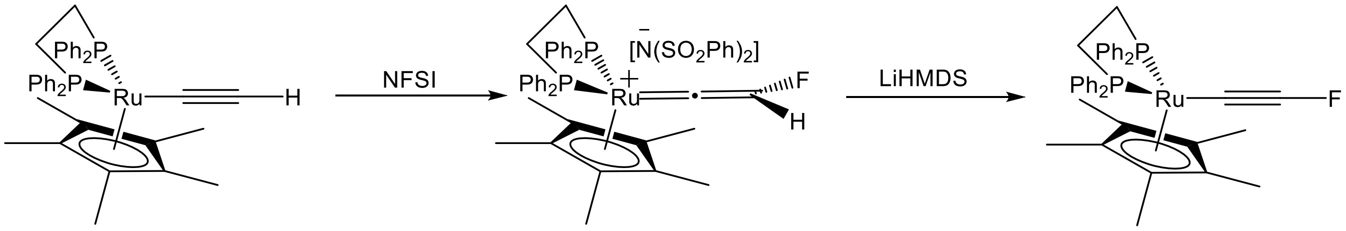

**Scheme 1.11** Synthesis of a fluoroalkyne.

The fluoroalkynyl is an example of only a handful of C(sp)-F bonds owing to their high reactivity and at room temperature dimerization can occur. Fluorinated alkynes show a particular increased reactivity compared to the hydrogen substituted analogue as the dimerization transition state is at low energy and the dimerization product is thermodynamically more stable than the terminal alkyne and so this route is preferred. However, no dimerization in this example was observed. Having shown that OSEF is an effective mechanism for forming C-F bonds, this research project is looking to extend this mechanism to pincer complexes.

## 1.2 Introduction to Pincer Ligands

Pincer ligands have become ubiquitous in organometallic chemistry in recent years with several reviews detailing their use in synthesis, bond activation and catalysis.[21–24] Pincer ligands can be defined as tridentate ligands that upon coordination to the metal centre give a well-defined meridional geometry and based on their donor character to the metal centre can be classified into three groups: neutral $L_3$, monoanionic $L_2X$ and dianionic $LX_2$ (rare).[22] The ability of the pincer ligand to stabilise metal centres and the flexibility it offers makes the corresponding complexes highly desirable in various organic transformations and bond functionalisations. A property of pyridine-based pincer ligands that makes them highly desirable is the aromatisation-dearomatisation mechanism. In this mechanism the benzylic arm of the ligand is deprotonated along with dearomatisation of the central pyridine ring. The oxidation state of the metal remains the same as the central N atom is now an amide donor to the metal. Upon reaction with a substrate the aromatised complex is reformed. Another appealing property of pincer ligand is that the ligand can be easily modified to give different steric/electronic properties to enhance the catalytic activity of the pincer complex. This section will outline the common modifications made to pincer ligands and the subsequent effect this can have on the reactivity on the metal complex.

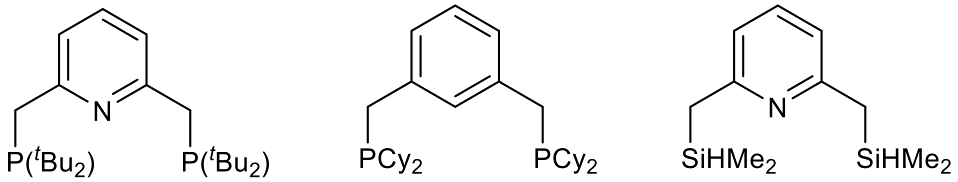

**$L_3$** **$L_2X$** **$LX_2$**

**Figure 1.5** Examples of previously synthesised $L_3$, $L_2X$ and $LX_2$ pincer ligands.[25–27]

### 1.2.1 Modification of Pincer Ligands

Modification of pincer ligands, whether it be the central donor atom, linker groups or flanking groups is a simple method to influence the steric and electronic properties of the metal complex which in-turn has an effect on the reactivity. Figure 1.6 shows the general structure of a metal complex with a coordinated pincer ligand.

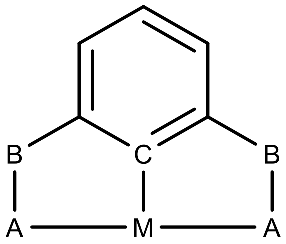

**Figure 1.6** General structure of pincer complex.

Modification of ‘A’ by introducing new donor atoms such as P,N or S affects the steric bulk around the metal centre for example *ᵗ*Bu groups give greater steric hindrance around the metal centre compared to $Et_2$ or even H in some examples. The nature of these groups also impacts the donor nature of ‘A’. By employing different ‘A’ groups an asymmetric pincer complex such as PNN can be synthesised and this technique has been shown to greatly increase the catalytic activity of a complex. Modification of position ‘B’ impacts the reactivity of the complex, as if atoms such as oxygen are used in place of $-CH_2-$ groups this means the metal-ligand cooperation mechanism via dearomatisation-aromatisation cannot take place and so a different method of reactivity is observed. Asymmetric pincer ligands with different substituents at the ‘B’ position are rare due to synthetic difficulties with some synthetic routes containing 10 or more steps. The final modification that can be made to pincer ligands is to change the central donor atom. A common example of this is replacing nitrogen with carbon, main group elements such as boron and silicon have also been used as donor atoms. Using carbon as the central donor atom offers unique reactivity as these complexes do not undergo dearomatisation-aromatisation unlike the nitrogen-based complexes, boron and silicon are interesting examples as boron is a greater σ-donor compared with nitrogen or carbon. Silicon forms strong bonds with metals allowing the stabilisation of reactive intermediates.

### (i) Modification of Flanking groups

Modification of the flanking group is done at the beginning of the synthesis through careful choice of reagent. The highly electron donating PNP ligand reported by Milstein *et al.* uses chloromethyl di-substituted pyridine which is then treated with the desired phosphine species, in this case di-tert butyl phosphine, to yield the $^t$Bu-PNP ligand.[28] A slightly modified route to the $^t$Bu-PNP ligand was reported in 2018 in which di-substituted 2,6-lutidene is deprotonated at both methyl groups followed by addition of di-tert butyl chlorophosphine.[29] Through modification of either of the synthetic routes described above PNP type ligands bearing different R groups on the phosphines can be produced by choice of the phosphine reagent added. For example in place of di-tert butyl phosphine to give $^{t}$Bu-PNP, diisopropylphosphine or diphenylphosphine can be used to yield the iPr-PNP and Ph-PNP ligands respectively.[30,31,32]

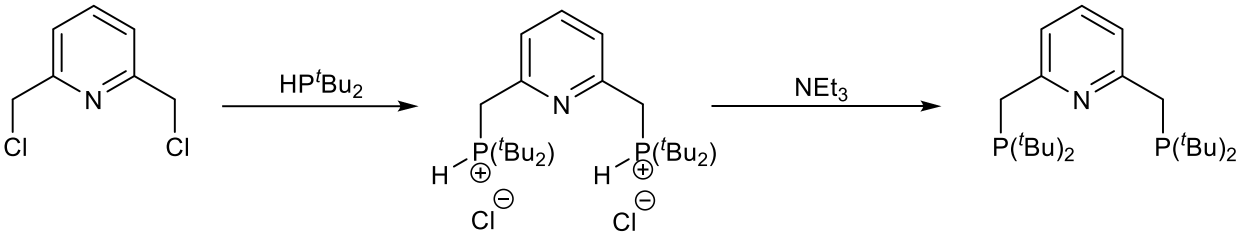

**Scheme 1.12** Reported synthetic route to $^{t}$Bu-PNP ligand.

The synthesis of the unsymmetrical ligand PNN where one phosphorus donor is replaced with a nitrogen with two ethyl groups attached has been described.[30] Replacing the phosphorus to form the PNN ligand has been shown to have a significant catalytic benefit which will be discussed in section 1.2.2. The synthesis of the PNN ligand begins with 2,6-bis(chloromethyl)pyridine and this was treated with NBS and AIBN to form 2-bromomethyl-6-methylpyridine to which diethylamine was added to form the intermediate species shown in scheme 1.13. The methyl group of the intermediate species was deprotonated with $^{n}$BuLi followed by addition of the phosphine species, di-tertbutylchlorophosphine to yield the PNN ligand after extraction and purification.[30] It is clear that the synthesis of the unsymmetrical ligand PNN is significantly more complicated compared with the synthesis of the PNP species described above.

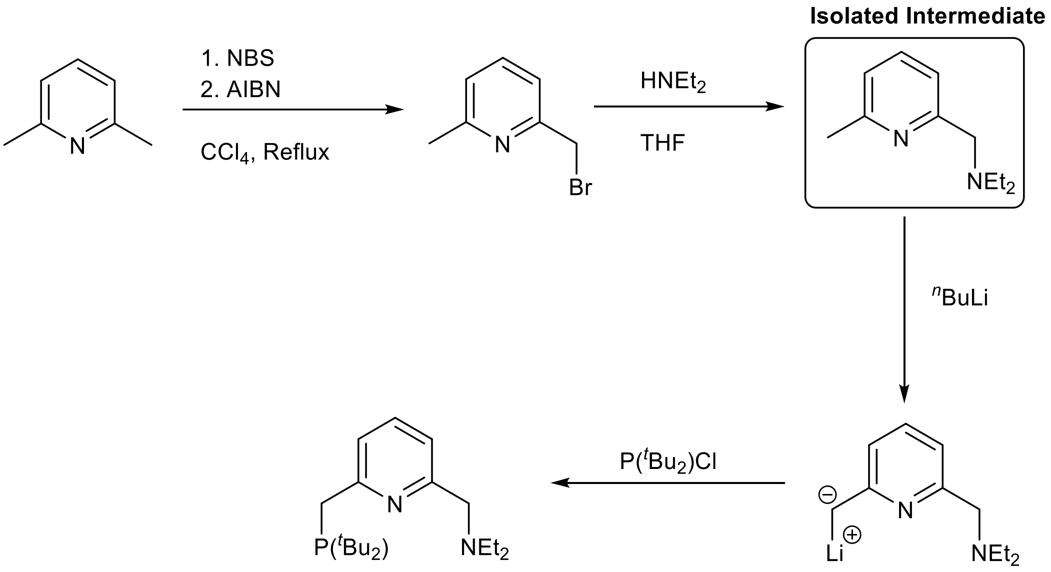

**Scheme 1.13** Synthetic route to PNN.

Another PNN ligand has been described in the literature, however, in this case the ligand is based on bipyridine.[33,34]

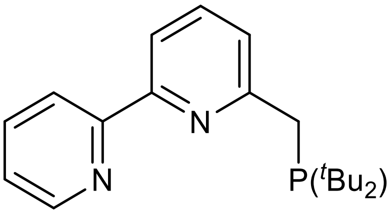

**Figure 1.7** BPy-PNN ligand

The ligand shown in figure 1.7 was synthesised by adapting the procedure for the PNP ligand synthesis shown in scheme 1.12.[33] Whereas 2,6-lutidene was used for the PNP synthesis in this case the chloromethyl substituted bipyridine species was used, to which di-tert butlyphosphine was added to form the phosphonium salt which was deprotonated with triethylamine to form the BPy-PNN ligand. Although phosphorus and nitrogen-based groups dominate pincer ligand chemistry there are also examples of other elements being used such as sulfur and oxygen.[35,36]

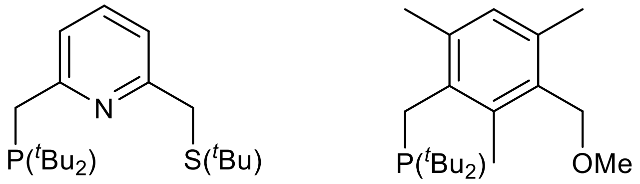

**PNS** **PCO**

**Figure 1.8** Structure of PNS and PCO pincer ligands.

The synthesis of the PNS ligand uses 2,6-bis(chloromethyl)pyridine which was reacted with LiP$^t$Bu$_2$(BH$_3$) to form a phosphine-substituted species. Addition of sodium 2-methyl-2-propanethiolate resulted in substitution of the remaining chlorine with an S$^t$Bu group. The final step was the removal of the borane group from the phosphine species and this was done by refluxing in diethylamine to afford the PNS ligand shown in figure 1.8.[35] The synthesis of the PCO ligand begins with 1,3-bis(bromomethyl)-2,4,6-trimethylbenzene to which sodium methoxide is added to give the methoxy intermediate, di-tert-butylphosphine was then added to give the phosphonium salt as seen in previous ligand syntheses and after workup the desired PCO species was formed. Like with the synthesis of the PNN ligand, PNS and PCO require more steps to give the desired product compared with the PNP ligand which is only a two-step process with an easier workup and purification process.

### (ii) Modification of Ligand Backbone

Modifying the ligand backbone by changing the linker groups has also been investigated, as this influences the reactivity of the metal complex in catalysis and bond activation. Examples of ligands with modified ligand backbones include the PONOP ligand in which the -CH$_2$- groups in the backbone are replaced by ether oxygen atoms and also the use of -NR- groups.[37–41] Whereas the modification of the donor groups is dependent on the reagent (PR$_2$/NR$_2$) in the case of changing the atoms linking the ancillary ligands with either the pyridine/benzene donor group is dependent on the precursor used for the reaction. The synthesis of the PONOP ligand was first reported by Milstein and co-workers in 2009 using 2,6-dihydroxypyridine hydrochloride as a precursor compared to the chloromethyl disubstituted pyridine used for the PNP and PNN ligands.[28,30] The hydroxypyridine species was treated with tetramethylethylenediamine (TMEDA) and trimethylamine (TEA) followed by addition of the required phosphine species, in this example diisopropylphosphine and di-tert butylphosphine were used to yield either the iPr-PONOP or ${}^{t}$Bu-PONOP species respectively.[38]

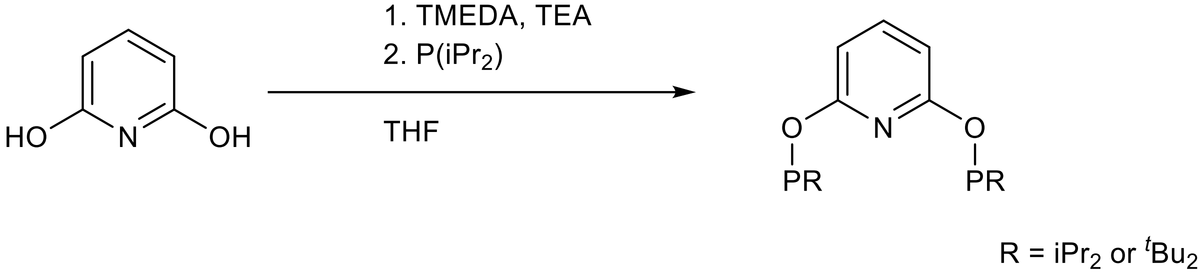

**Scheme 1.14** Synthesis of the PONOP ligand.

Bernskoetter *et al.* reported a different synthetic route to the one shown above, all reagents used in the reaction were the same apart from TMEDA which was not added instead the length of time the reaction was stirred for was increased to one week. While this did yield the PONOP complex it showed a significantly reduced yield (57 %) compared to the procedure reported by the Milstein group (76 %).[42] By combining elements of each of the synthetic routes to the PONOP ligand described above, Kundu *et al.* combined all reagents in a one-pot synthesis (TMEDA, TEA and phosphine reagent) and left the reaction to stir for one week which after purification gave an 85% yield and an improved purity.[43]

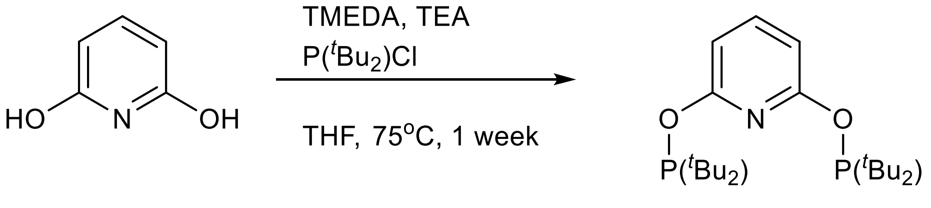

**Scheme 1.15** Improved synthesis of PONOP ligand.

Pincer ligands bearing amine groups in place of -$CH_2$ or -O- in the ligand backbone have also been synthesised employing similar syntheses to the ones seen for the PNP and PONOP ligands.[39–41,44,45] The first example of these ligands to be synthesised using -NH- groups was reported by Benito-Garragori *et al.* in 2006 based on diaminopyridine.[37] The synthesis is relatively straightforward by treatment of diaminopyridine with the required chlorophosphine species in the presence of either $NEt_3$ or $^n$BuLi to yield the desired ligand shown in figure 1.9.

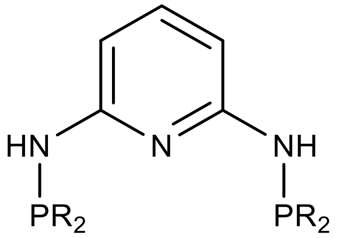

**Figure 1.9** Structure of PNP ligand with -NH- linker groups.

He *et al.* reported the synthesis of an asymmetric pincer ligand with one arm of the ligand bearing an -NH- group.[41] The synthetic route is similar to that described for the PNN ligand above as in this reaction a similar species as the isolated intermediate in scheme 1.14 is used, however, the methyl group is replaced with an amino group. The intermediate species is treated with P($^t$Bu$_2$)Cl, $NEt_3$ and $^n$BuLi (scheme 1.16).[41]

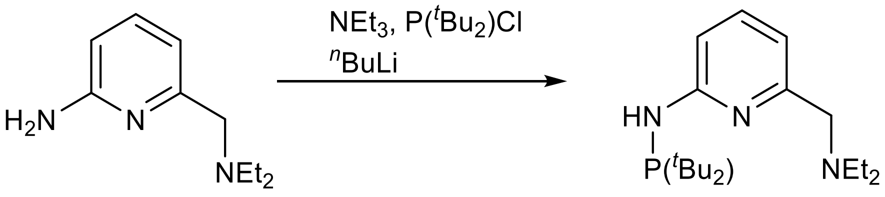

**Scheme 1.16** Synthesis of asymmetric P$^{NH}$NN ligand.

### (iii) Modification of Central Donor Atom

Modification of the central donor atom is a straight-forward process as this can be changed through selection of the starting material. For example, nitrogen-donor ligands such as PNP and PNN are based on disubstituted pyridines and carbon donor ligands such as PCP are derived from disubstituted benzenes.[46,47] However pincer ligands with boron- and silicon-based species as the central donor atom have been investigated owing to their unique properties compared with nitrogen and carbon.[48–51] Boron is a stronger σ-donor than carbon and nitrogen and so has stronger electron releasing properties, which can be beneficial in organic transformations and bond functionalisations making pincer ligands containing a central boron an appealing prospect. The first example of a tridentate boryl ligand was reported by Segawa *et al.* in 2009. The hydroborane pincer ligand was formed by the reaction of di-tertbutylphosphine with a diamine to form the diphosphine substituted species shown in scheme 1.17. The intermediate was treated with an excess $BH_3.SMe_2$ to give a phosphine-boron compound which was treated with n-$Pr_2NH$ to give the PBP ligand.[49]

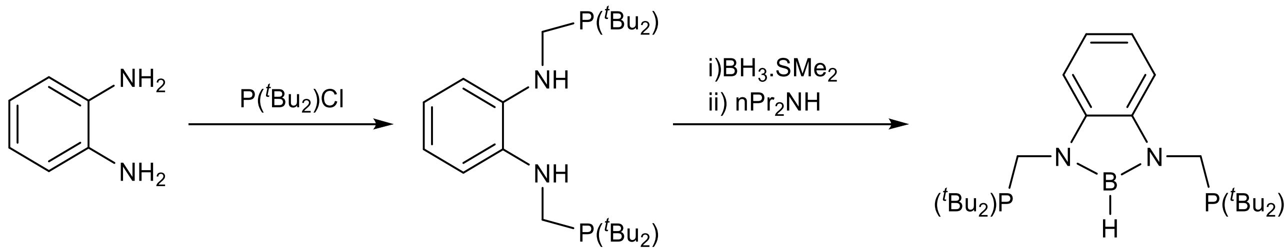

**Scheme 1.17** Synthetic route to PBP ligand.

The introduction of a silicon-based group is also interesting as Si-M are characteristically strong which can aid in the stabilisation of reactive intermediates formed in a catalytic cycle. In 2001 Stradiotto *et al.* reported the synthesis of a silane pincer ligand formed by the reaction between methyldichlorosilane and 8-lithioquinoline.[48] Another class of Si pincer ligands have also been reported by the Milstein group. The PSiP ligand was synthesised by the lithiation of di-isopropyl(ortho-bromophenyl)phosphine with $^{t}$BuLi and the resultant product coupled with $SiCl_4$ followed by a reduction of the intermediate with $LiAlH_4$ to yield the PSiP ligand.[51]

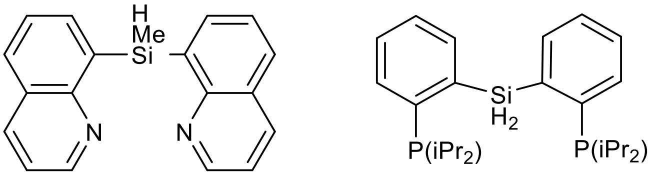

**Tilley 2001** **Milstein 2008**

**Figure 1.10** Structures of previously synthesised Si-containing pincer ligands.

## 1.2.2 Reactivity of Pincer Complexes

In 2005 Zhang *et al.* published a paper in which they were attempting to form a Ru(0) PNN complex from the corresponding Ru(II) species by treatment with a base, what they discovered is rather than form the Ru(0) species the benzylic arm is deprotonated, which results in dearomatization of the central pyridine ring. This dearomatized species has been shown to activate a variety of polar and non-polar bonds including H-H,[30] H-OH,[52] B-H,[53] and N-H,[54] upon activation of the bond the six coordinate aromatized ligand is reformed. The formal oxidation state of the metal centre remains the same during dearomatisation-aromatisation, as in the dearomatised complex the central N atom becomes an amide donor to the metal so is now an $L_2X$ type ligand.

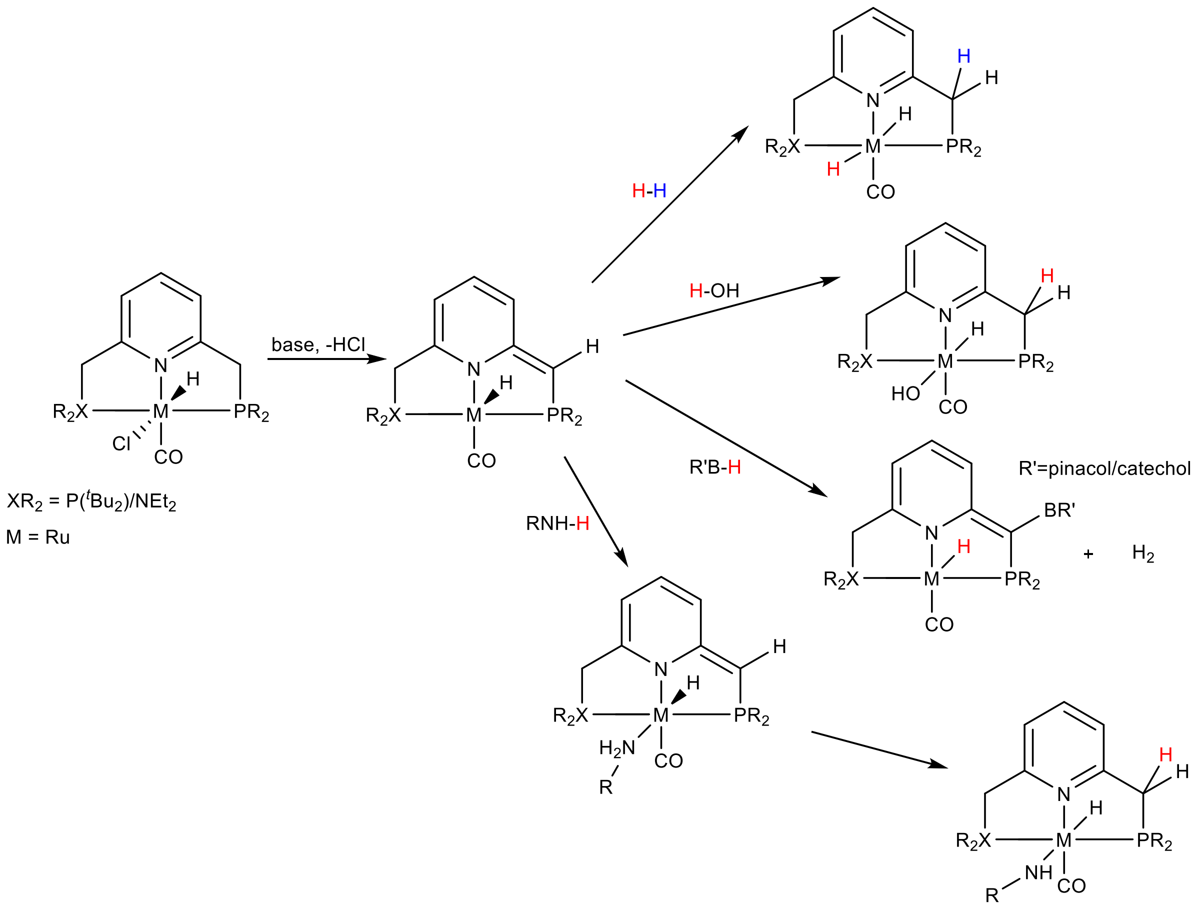

**Figure 1.11** Examples of bond activation using a dearomatized pincer complex.

The dearomatized intermediate shown in figure 1.11 has also been used extensively in catalytic reactions such as hydrogenations, dehydrogenations and catalytic cross couplings.[23,30,34,53,55–58,59]An example of the dearomatization-aromatization mechanism being used in catalysis is in the dehydrogenative coupling of alcohols to form esters catalysed by the dearomatized Ru(PNN) complex.[30]

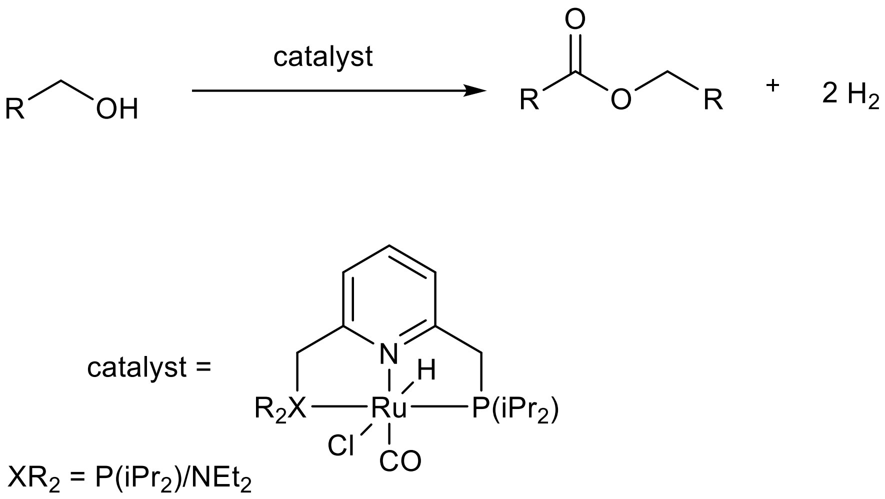

**Scheme 1.18** Catalytic dehydrogenation of alcohols to form esters.

The dearomatized PNN complex showed the greatest catalytic activity with the corresponding ester being obtained in greater than 90% yield compared with 67.2% when the PNP equivalent was employed as a catalyst. This increase in activity can be attributed to the hemilabile amine arm, which can dissociate from the metal centre allowing coordination of the substrate.[30] In an attempt to increase the catalytic activity of the PNP complex -NH- linker groups were employed in place of -$CH_2$- (figure 1.9) as the -NH- group is more acidic and so dearomatization is favoured. The PNP complex with -NH- linker groups was employed as a catalyst in the transfer hydrogenation of ketones.[40]

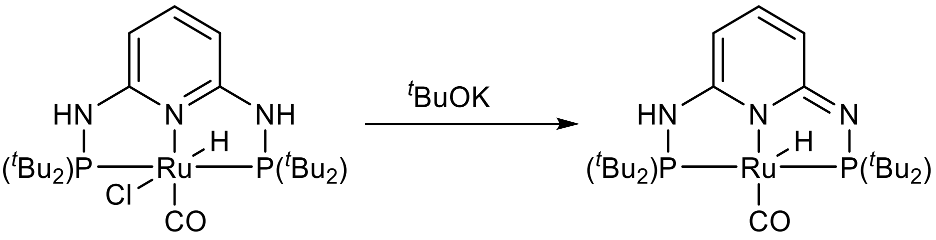

**Scheme 1.19** Deprotonation and concomitant dearomatization of PNP complex.

Both the aromatized and dearomatized complexes were used as catalysts, however, no reaction was observed for the aromatized complex showing the dearomatized species is the active catalyst. Cyclohexanone was employed as the substrate and after 16h with the dearomatized complex used as the catalyst full conversion to cyclohexanol was achieved. Carrying out the reaction at milder temperatures (42°C from 80°C) also showed full conversion to the alcohol, however, the length of the reaction had to be increased.[40]

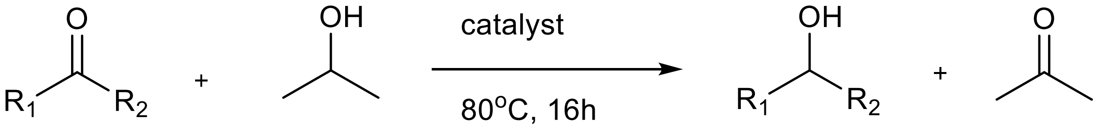

**Scheme 1.20** Transfer hydrogenation of ketones.

While the PNS complex (figure 1.12) is analogous to the PNN and PNP complexes described previously, upon treatment with *ᵗ*BuOK the desired deprotonated species is not formed but rather a new dimer complex forms in which the central Ru atoms are bound to the opposite sulfur benzylic arm.[35]

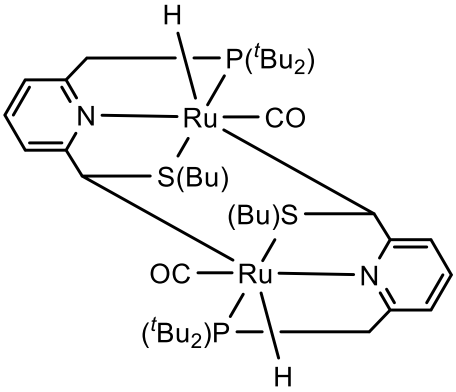

**Figure 1.12** Dimeric complex formed upon treatment of PNS complex with base.

Any attempts to isolate and characterise the dearomatized the PNS complex were unsuccessful, as in each case the dimer shown above was observed. It is believed that the dimer is seen for the PNS complex and not the PNP and PNN complexes due to the lack of steric bulk around the S(Bu) group compared with $^t$Bu$_2$ or NEt$_2$. Despite being unable to isolate the dearomatized complex the aromatized PNS complex was used as a catalyst in the coupling of amines with alcohols to form amides. A one-pot synthesis in which the PNS complex, benzylamine, hexanol and base (KMDS) were all heated at reflux was carried out. Surprisingly, the corresponding amide was formed in 46% yield, which is similar to that obtained for the dearomatized PNN complex. This is further evidence that introducing a hemilabile arm like NEt$_2$ or SBu into the pincer ligand greatly increases the catalytic activity.[35]

The dearomatization-aromatization mechanism shown above does not apply to all pincer complexes, such as benzene-based complexes (PCP) and those with ether -O- atoms (PONOP) in the ligand backbone or substituted N atoms (-NR-). Although these complexes cannot undergo dearomatization-aromatization they still display good catalytic activtity.[38,45,50,60,61] An example of this is in the dehydrogenation of formic acid which is catalysed by an Fe pincer complex with -NMe- linker groups in the ligand backbone. In this example the complex is treated with a base to abstract the bromide from the metal centre to form the catalytically active coordinatively unsaturated species which is analogous to the dearomatized complexes. Without the addition of base no reactivity toward formic acid was observed.[61]

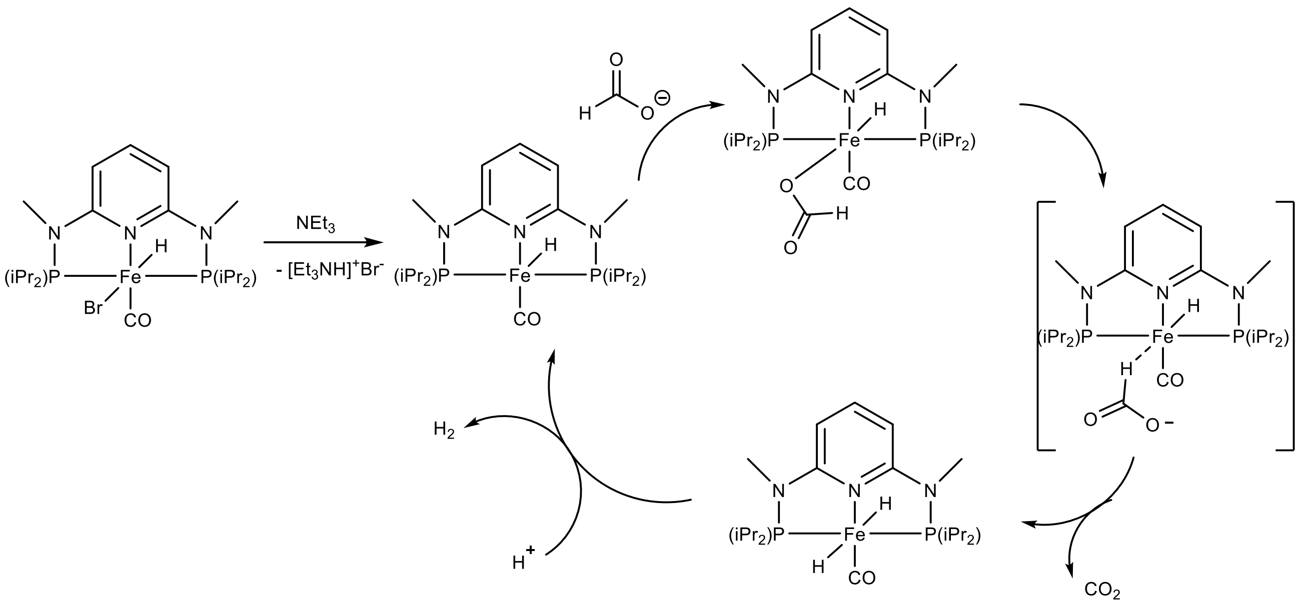

**Scheme 1.21** Catalytic cycle for the dehydrogenation of formic acid.

PONOP-based pincer complexes have also been used as catalysts in reactions such as hydrogenation and transfer hydrogenation. Mazza *et al.* reported the catalytic use of a Fe-PONOP complex in the hydrogenation of aldehydes.[60]

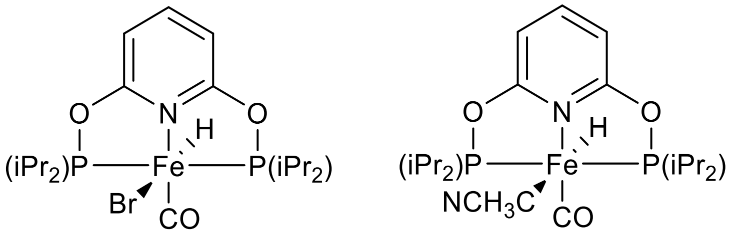

**Figure 1.13** Fe-PONOP complexes used in the hydrogenation of aldehydes.

Initially the complexes shown in figure 1.13 were investigated for their ability to activate hydrogen as previously demonstrated by the dearomatized pincer complexes. Both complexes were able to activate hydrogen, shown through H/D exchange reactions in which the hydride is exchanged for deuterium. The Fe-PONOP complexes showed reduced activity compared to the dearomatized species as it took 150h for 50% exchange to be observed, however, this could be reduced to 10 minutes by using $d_4$-methanol as a solvent in place of $d_8$-THF. In the hydrogenation of aldehydes the complex bearing an acetonitrile ligand showed no activity toward hydrogenation, however, when the brominated species was employed under a $H_2$ atmosphere with the aldehyde, the corresponding alcohols were obtained in yields greater than 90%.[60] Aldehydes with electron withdrawing and donating substituents were hydrogenated in good yields, aliphatic aldehydes were also hydrogenated to alcohols however in significantly lower yields (approximately 60%).

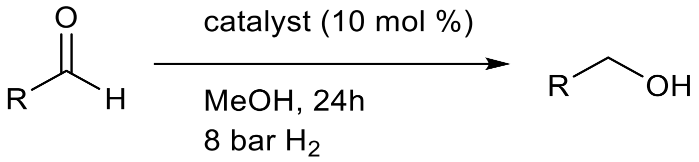

**Scheme 1.22** Hydrogenation of aldehydes catalysed by an Fe-PONOP complex.

As shown in this section pincer ligands can be modified by changing the flanking groups, linker groups and the central donor atom and by doing this a significant effect on reactivity is seen. However, currently modification of pincer ligands is done through the design of a synthetic route with careful choice of reagents as described in section 1.2.1. There are very few examples within the literature of substituents being added into the pincer ligand backbone to form an asymmetric complex and subsequent characterisation of this complex along with reactivity studies. A potential reason for this could be due to the fact that modification of the pincer ligand at the central donor atom or the flanking groups is more achievable experimentally as asymmetric complexes have proven to be challenging to synthesise. Also, modification of these groups has been shown extensively to influence the reactivity of the complex and for this reason this area has been the focus of researchers.

# 2. Aims

The aims of this research project were to exploit the dearomatisation-aromatisation mechanism of a PNP type pincer ligand to successfully synthesise a novel asymmetric pincer complex containing a C-F bond within the ligand backbone. Thereby extending the scope of the outer-sphere electrophilic fluorination mechanism. To introduce carbon- and silicon-based groups into the ligand backbone and fully characterise the newly synthesised complexes. The purpose of introducing these groups into the ligand backbone is to improve the known synthetic procedures for asymmetric pincer complexes as outlined in section 1.2.1. To interrogate the structure of these complexes to determine what affect the introduction of these groups has on the geometry of the coordinated ligands around the metal centre. To investigate the onward reactivity of the resultant complexes by assessing their ability to act as a base and how this can be improved by careful choice of either fluorine-, carbon- or silicon-based groups.  By assessing the onward reactivity of these modified complexes in a simple proton transfer reaction, it is hoped that this will demonstrate the potential to improve the catalytic performance of a pincer complex through careful choice of substituent introduced into the ligand backbone.

# 3. Results and Discussion

## 3.1 Synthesis of Precursors and Ru($^{tBu}$PNP) Complex

### 3.1.1 Synthesis and Characterisation of [RuHCl(CO)($PPh_3$)$_3$] (1).

The synthetic route to the ruthenium precursor complex, [RuHCl(CO)($PPh_3$)$_3$] was adapted from a previously reported literature procedure.[62] Scheme 3.1 shows the synthetic route to complex **1**.

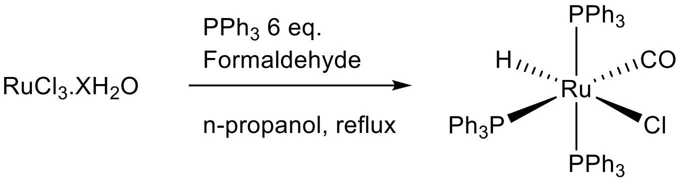

**1**

**Scheme 3.1** Synthetic route to [RuHCl(CO)($PPh_3$)$_3$].

The desired product was afforded by heating $RuCl_3.xH_2O$ at reflux with 6 eq. of triphenylphosphine in n-propanol. Formaldehyde was used as a solvent and acted as a carbonyl source and a reductant. The product obtained was characterised using $^1$H and $^{31}$P NMR spectroscopy and used without any further purification. The $^1$H NMR spectrum displayed a characteristic hydride signal at -7.20 ppm with a doublet coupling constant of 103.63 Hz and a triplet coupling constant of 21.67 Hz which is in agreement with previously reported literature data.[62]

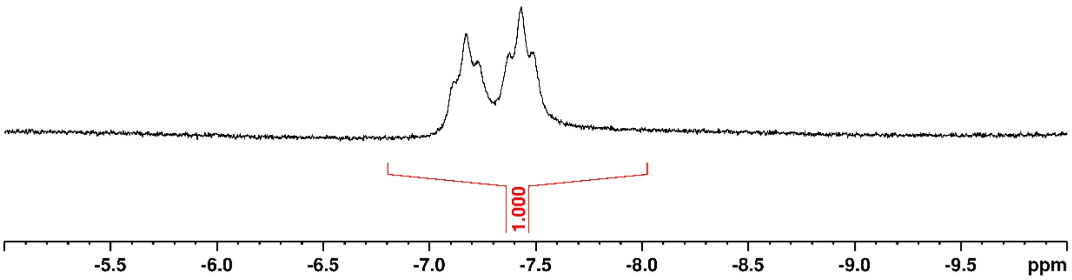

**Figure 3.1** $^1$H NMR spectrum of [RuHCl(CO)(PPh$_3$)$_3$] showing hydride signal.

A $^{31}$P{$^1$H} NMR spectrum was also recorded and is shown in figure 3.2. A signal was observed at 39.96 ppm with an integration of 2 and a second at 13.04 ppm with an integration of 1 and these values agree with previously unpublished work. The impurity observed at approximately 29 ppm can be assigned to triphenylphosphine oxide.

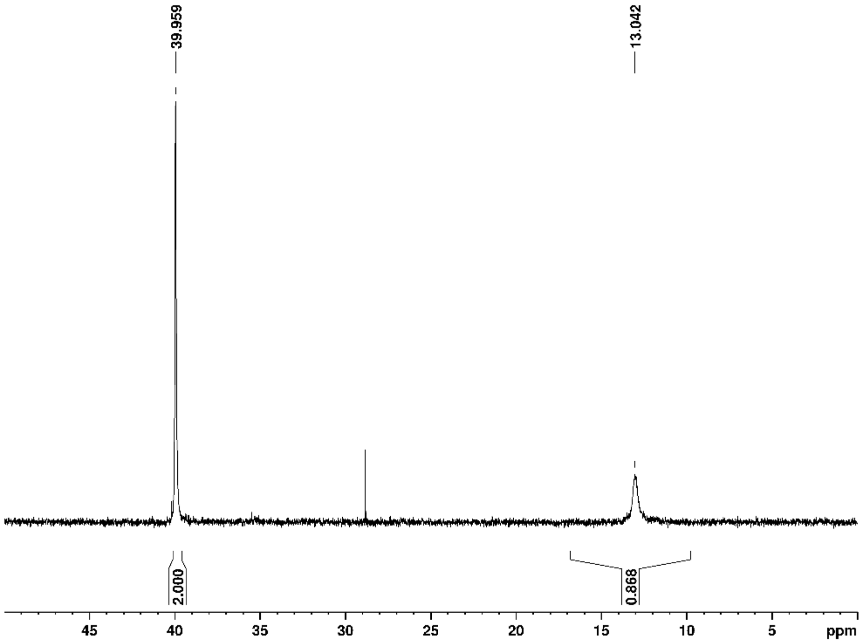

**Figure 3.2** $^{31}$P{$^1$H} NMR spectrum of [RuHCl(CO)(PPh$_3$)$_3$].

### 3.1.2 Synthesis and Characterisation of $^{tBu}$PNP (2).

The synthesis of the ligand precursor $^{tBu}$PNP was adapted from a previously reported literature procedure.[29] The ligand precursor, $^{tBu}$PNP (**2**), was prepared by adding 2 equivalents of $^{n}$BuLi to 2,6-dimethylpyridine to deprotonate the two methyl arms and form the intermediate species shown in scheme 3.2. Di-tert-butyl-chlorophosphine was then added to yield 2,6-bis((di-tert-butylphopshino)methyl)pyridine ($^{tBu}$PNP), **2**.

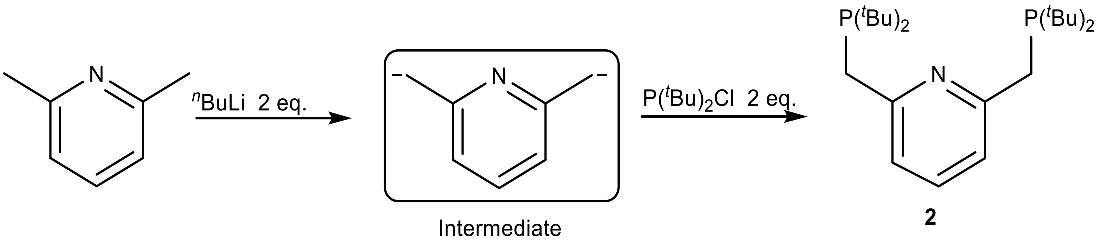

**Scheme 3.2** Synthetic route to ligand precursor, $^{tBu}$PNP.

$^{1}$H and $^{31}P\{^{1}H\}$ NMR spectroscopy were used to analyse the crude product before any purification had been carried out. Figure 3.3 shows the $^{31}$P spectrum of crude **2**. As both phosphorus nuclei within **2** are equivalent only one resonance should be observed. The spectrum shows the expected singlet at 36.1 ppm however an additional resonance can be observed at 164.7 ppm which suggests that unreacted $P(^{t}Bu_2)Cl$ is present in the crude product.

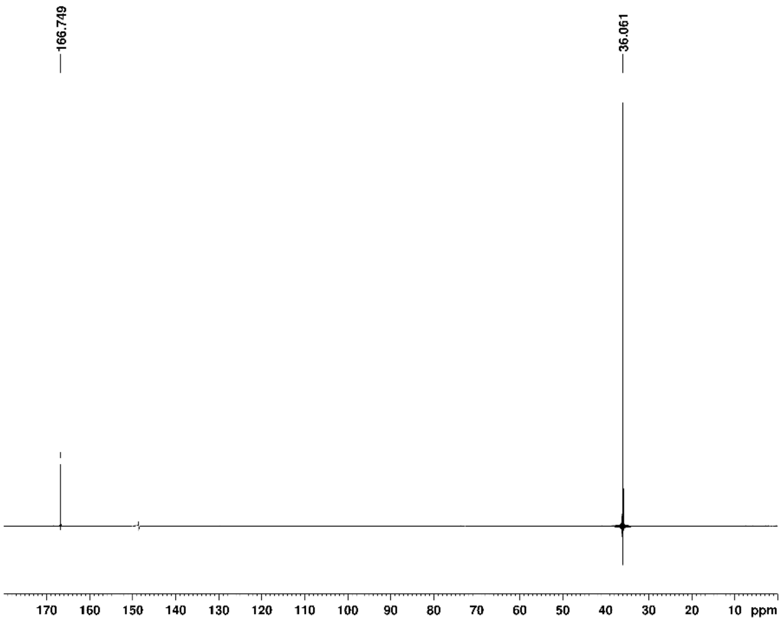

**Figure 3.3** $^{31}P\{^1H\}$ NMR spectrum of crude $^{tBu}$PNP. $D_2$ - dichloromethane was used as the NMR solvent.

In order to purify the crude **2** it was first washed with ice cold pentane to remove any unreacted $P(^tBu)_2Cl$ and then recrystallised from hot diethyl ether to give off white needle-like crystals which were analysed again using $^1H$ and $^{31}P\{^1H\}$ NMR spectroscopy. The $^{31}P\{^1H\}$ spectrum of purified **2** now only showed a singlet resonance at 36.1 ppm, as expected, and is agreement with data from the literature (Figure 3.4).[28]

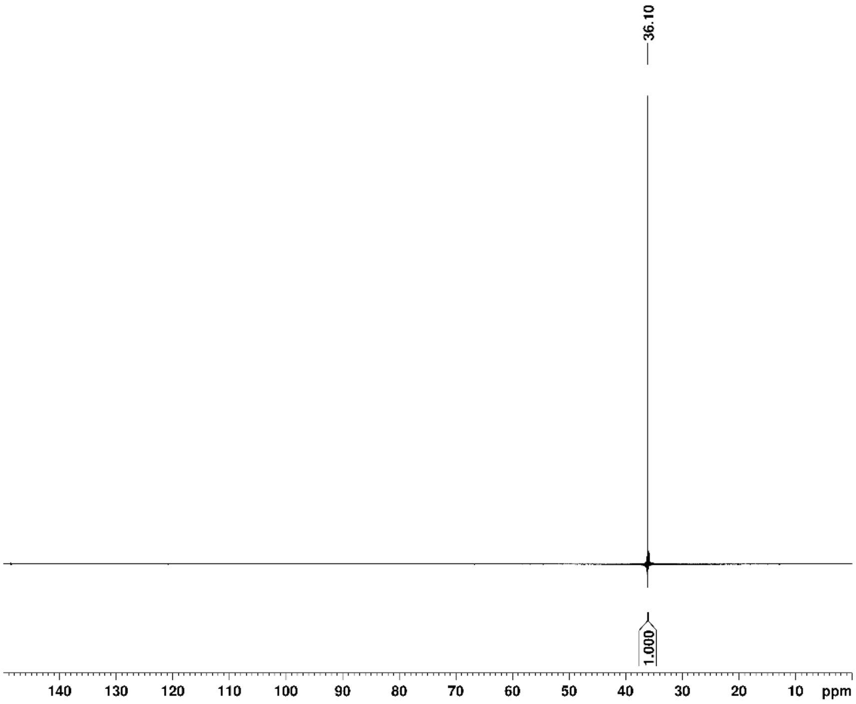

**Figure 3.4** $^{31}P\{^1H\}$ spectrum of purified **2**.

The $^1H$ spectrum of **2** is also in good agreement with the literature and is shown in figure 3.5.

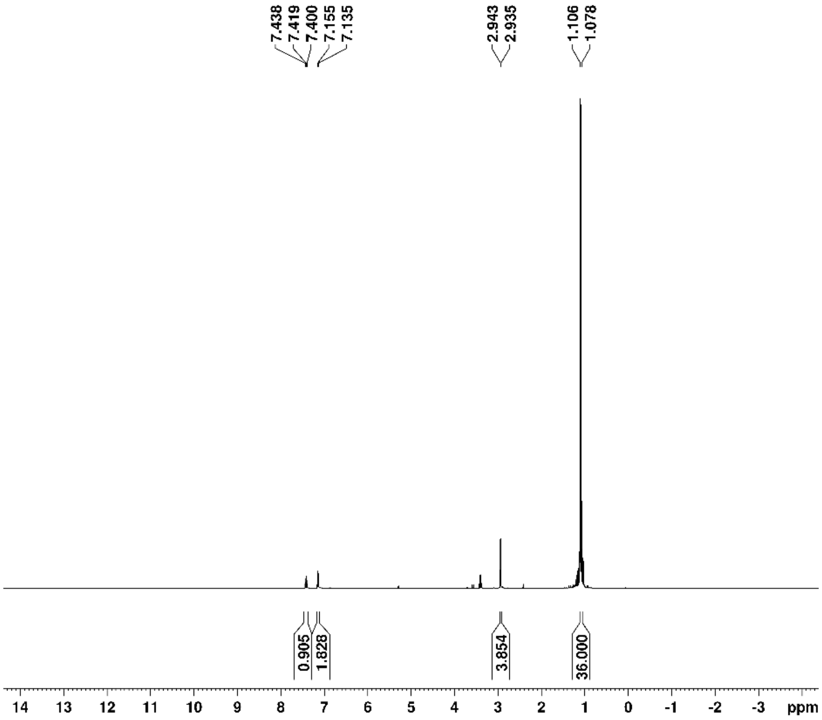

**Figure 3.5** $^1H$ NMR spectrum of **2**.

The spectrum shows a doublet at 1.1 ppm which was assigned to the identical t-butyl groups as shown through the integration value of 36. The doublet (10.99 Hz) splitting pattern is due to $^3J$ coupling to the phosphorus atom. The signal for the two $-CH_2$ groups in the ligand backbone can also be seen as a doublet resonance at 2.94 ppm and the splitting shows coupling between the -C**H** proton and phosphorus. The aromatic region is also well-defined shows expected signals, doublet and triplet at 7.14 ppm and 7.42 ppm respectively with the correct integration.

### 3.1.3 Synthesis and Characterisation of [RuHCl(CO)($^{tBu}$PNP)] (3).

The synthesis of the desired pincer complex, **3**, was adapted from a previously reported literature procedure.[29] Complex **3** was synthesised by adding the ligand ,**2**, to the complex ,**1**, in THF and heating for four hours at 65°C (Scheme 3.3).

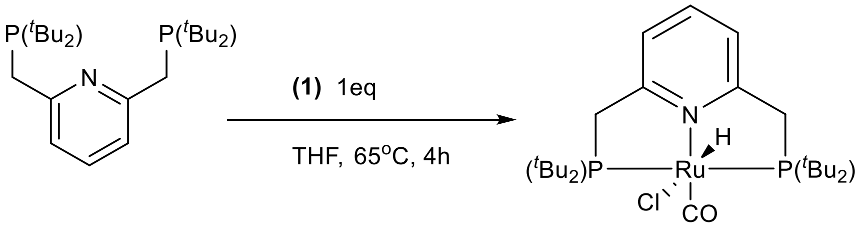

**3**

**Scheme 3.3** Synthetic route to [RuHCl(CO)($^{tBu}$PNP)].

Purification of **3** was achieved through slow diffusion of pentane into a THF solution of the complex. Figure 3.6 shows the $^{31}P\{^1H\}$ NMR spectrum of purified **3.**

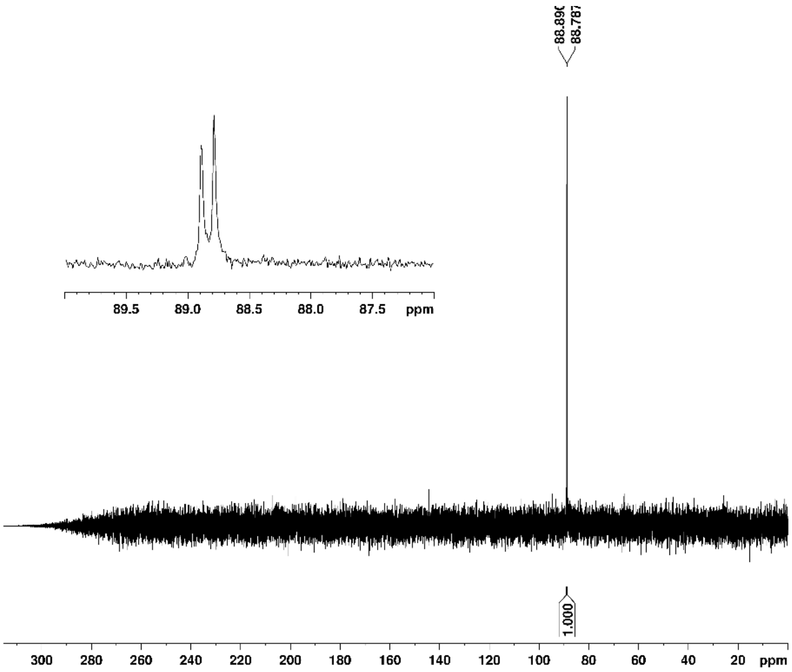

**Figure 3.6** $^{31}P\{^{1}H\}$ NMR spectrum of recrystallised **3**.

Figure 3.6 shows that full conversion of the precursors (**1** and **2**) to the desired product **3** has been achieved as no signal corresponding to these compounds can be seen in the spectrum. The spectrum shows a single resonance that would be expected for complex **3**. The signal appears as a doublet at 88.8 ppm however in the literature this is reported as a singlet, a reason for this could be due to the hydride signal being outside of the $^{1}$H decoupling region (0-10 ppm).

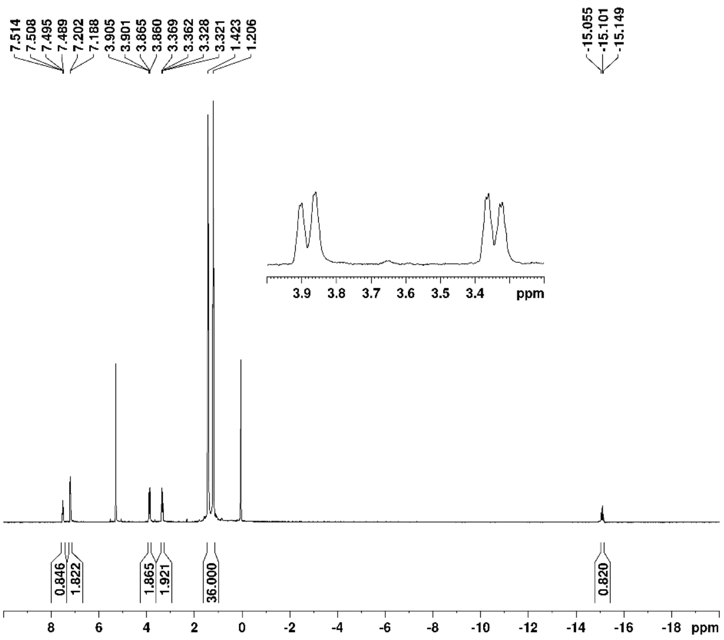

**Figure 3.7** $^1$H NMR spectrum of 3.

The $^1$H NMR spectrum shown in figure 3.7 confirms the formation of **3** as several characteristic signals can be identified. The spectrum shows the hydride signal as a triplet at -15.1 ppm which is shifted downfield from -7.2 ppm in the complex precursor (**1**). Due to the meridonal coordination of the PNP ligand and a lack of a plane of symmetry between P, N and P the tert-butyl protons aswell as the methylene protons of the benzylic arm are inequivalent. This can be seen in the $^1$H NMR spectrum as the methylene protons appear as roofed doublets at 3.35 and 3.88 ppm. However the tert-butyl protons are observed as two singlets at 1.42 and 1.20 ppm. The aromatic protons in the pyridine ring can be seen at 7.20 and 7.51 ppm.

## 3.2 Deprotonation and Subsequent Fluorination Reactions of 3

As described in section 1.2.2., pyridine-based pincer ligands have the ability to undergo a metal-ligand cooperation mechanism via dearomatisation-aromatisation of the central pyridine ring.[24,53,54] By deprotonating the methylene arm of the pincer ligand backbone a five coordinate unsaturated intermediate is formed which can then react with a variety of substrates.

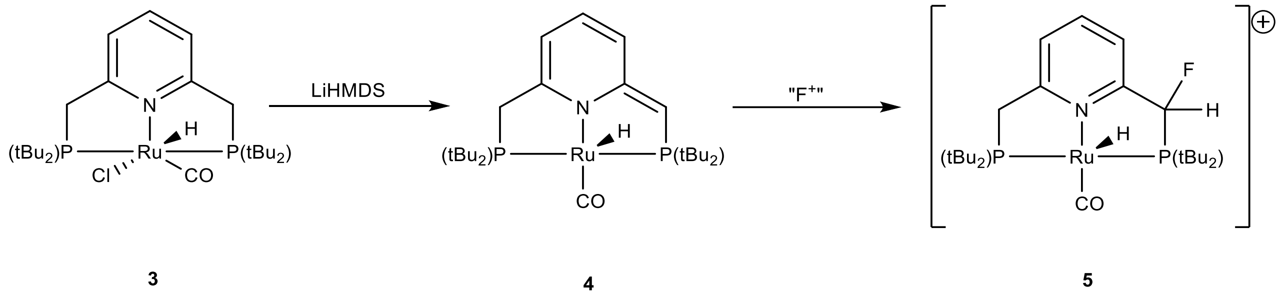

**Scheme 3.4** Synthetic route to of fluorinated pincer complex, **5**, via Metal-ligand Cooperation mechanism (MLC).

The first step of this process as shown in Scheme 3.4 is the formation of the dearomatized intermediate formed through deprotonation of the methylene arm using LiHMDS. Upon addition of a solution of LiHMDS in THF to a solution of **3**, an instant colour change from yellow to dark green was observed. A sample of the solution was removed, and a $^{31}P\{^1H\}$ NMR spectrum was recorded to confirm the formation of **4**

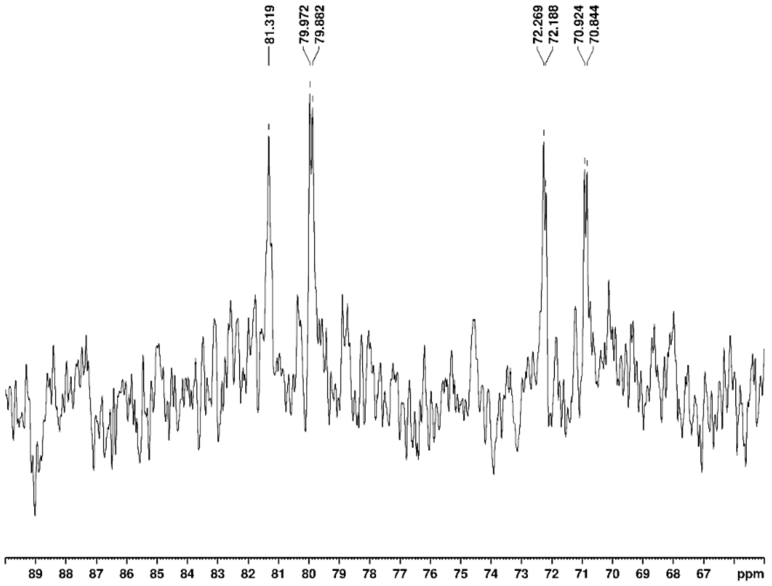

**Figure 3.8** $^{31}P\{^1H\}$ NMR spectrum of 3 after addition of LiHMDS.

The NMR spectrum shown in Figure 3.8 shows full conversion of **3** to **4** instantly upon addition of LiHMDS as no signal can be seen at approximately 89 ppm. The NMR spectrum shows an AB system of doublet of doublets, $^2J_{PP}$ = 217.54 Hz, indicative of two inequivalent *trans* phosphorus nuclei. Coupling between the phosphorus nuclei and the hydride is observed as the hydride signal lies outside of the decoupling region. With confirmation that the dearomatized species had been formed an electrophile was then added. Deprotonation and subsequent addition of the electrophile was carried out *in situ* due to sensitivity of the dearomatized complex toward moisture.

### 3.2.1 Fluorination with Selectfluor

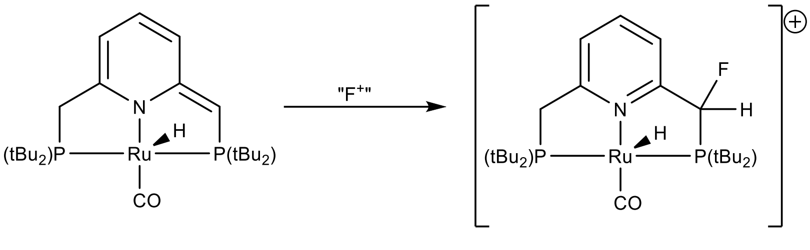

**4** **5**

**Scheme 3.5** Synthetic route showing formation of **5**.

The first step is to deprotonate the methylene arm of the pincer ligand as shown in scheme **3.4**. This was done by cooling the solution of **3** in THF and the base solution (LiHMDS in THF) using a salt-ice bath. Upon addition of the base solution to the complex solution a distinct colour change from yellow to dark green was observed and this is a good indication that deprotonation of **3** has occurred to give the dearomatized intermediate species, **4**, as shown in scheme 3.4. Once the colour change from yellow to dark green had been observed indicating formation of **4** one equivalent of selectfluor was immediately added and left to stir for 30 mins after which time the solution was concentrated under vacuum and analysed using $^{1}H$, $^{19}F$ and $^{31}P\{^{1}H\}$ NMR spectroscopy.

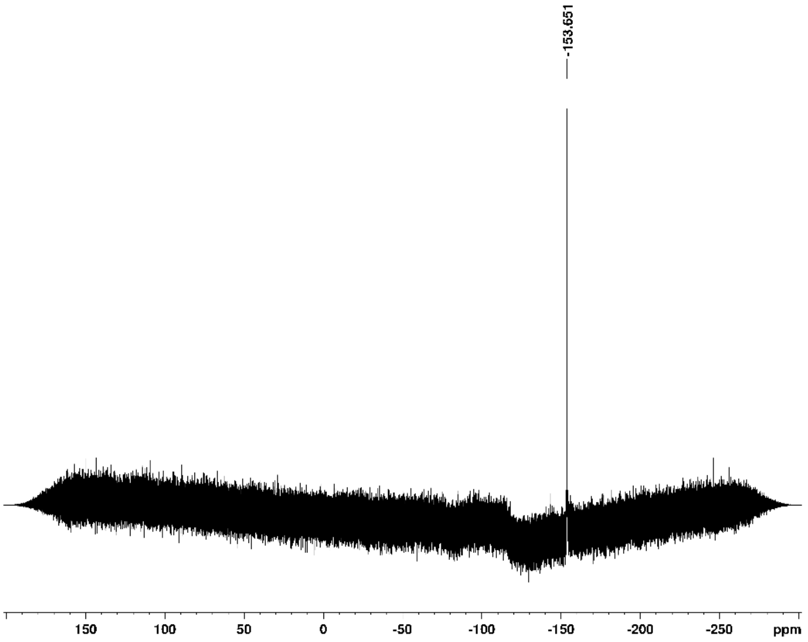

**Figure 3.9** $^{19}$F NMR spectrum of product obtained from fluorination reaction.

The $^{19}$F NMR spectrum shown in figure 3.9 shows no evidence of the formation of the fluorinated pincer complex (**5**). The resonance shown in the spectrum at -153.7 ppm was assigned to the tetrafluoroborate ($BF_4^-$) counterion which is present in selectfluor. Further experiments using selectfluor yielded similar results. A major indication from the $^{31}P\{^1H\}$ spectrum that a fluorine atom has been added in the ligand backbone is that in forming the fluorinated complex the two phosphines are now inequivalent. Therefore two resonances should be observed with a coupling between 200-300 Hz as this is charasteristic for a complex containing *trans* phosphorus atoms.

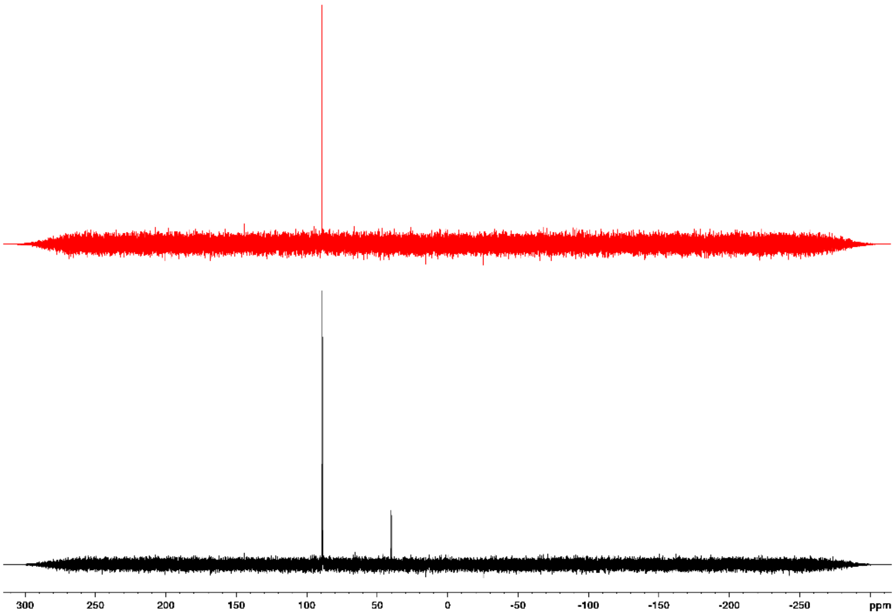

**Figure 3.10** $^{31}P\{^{1}H\}$ NMR spectra showing starting complex 3 (top) and the product obtained after addition of selectfluor (bottom).

The spectra shown in figure 3.10 show that fluorination of the pincer ligand backbone has not been achieved. The bottom spectrum shows that the deprotonated complex has been protonated as the signal at 88.9 ppm can be assigned to the pincer complex **3** as shown in the top spectrum. The singlet at approximately 40 ppm has not been identified. Mass spectrometry data also confirms the formation of **4a** due to the presence of a peak at m/z = 526.19 which is the mass of the reprotonated complex.

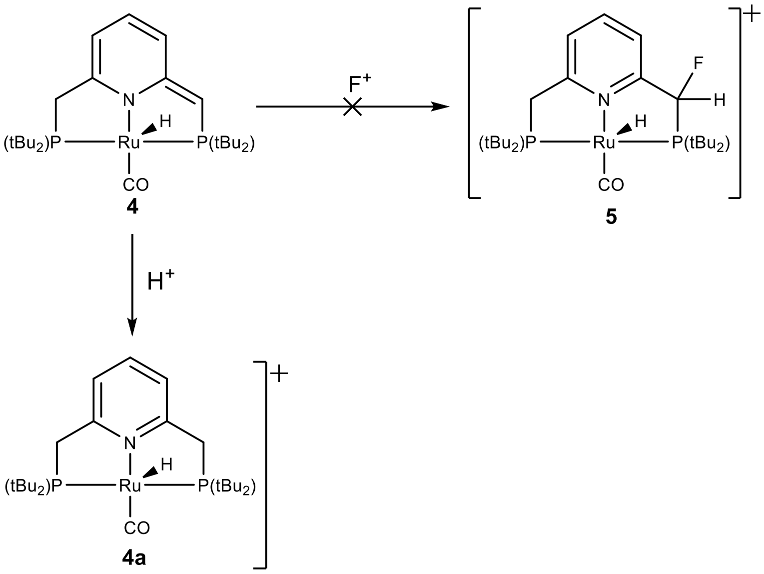

**Scheme 3.6** Reaction scheme showing formation of protonated species (4a) over fluorinated species (5).

### 3.2.2 Fluorination with N-fluorobenzenesulfonimide (NFSI)

The procedure for the deprotonation and subsequent fluorination using NFSI was carried out using the same method as described for selectfluor. NFSI does not suffer with the same poor solubility as selectfluor so reaction processes can be seen through NMR spectroscopy ($^1$H, $^{19}$F and $^{31}$P{$^1$H}).

Initially reactions with NFSI were unsuccessful as the main product formed was identified as the protonated complex (**4a**) as shown in scheme 3.6 and no evidence for the formation of **5** was observed.

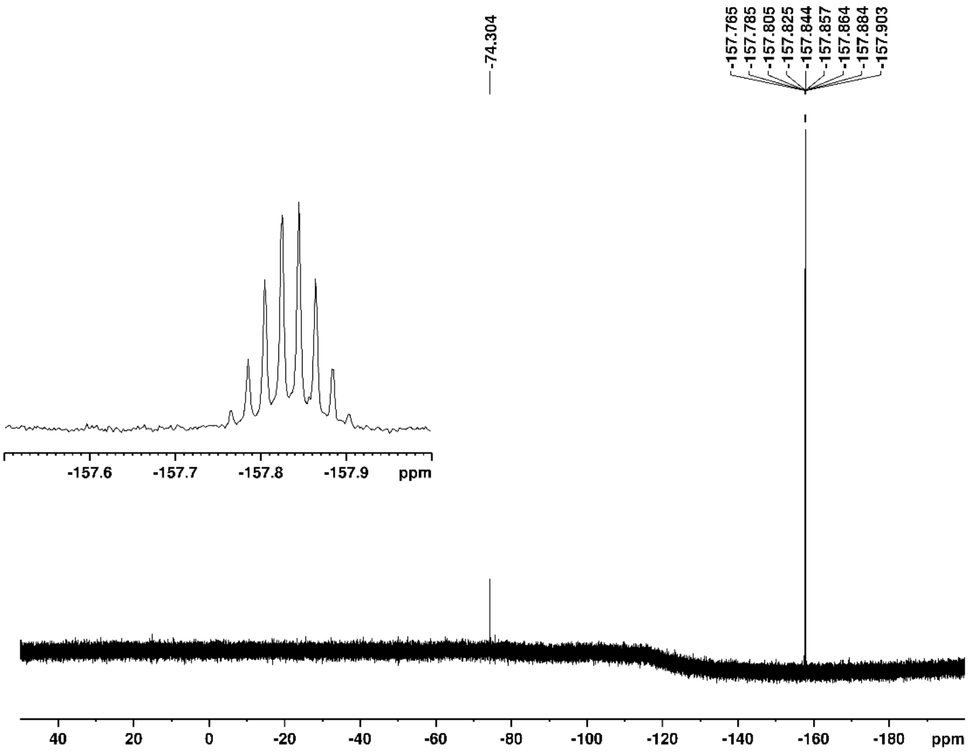

**Figure 3.11** $^{19}$F NMR of product obtained after addition of NFSI.

The $^{19}$F NMR spectrum in figure 3.11 shows no formation of **5** as the only visible resonances are a singlet at 74.3 ppm which can be assigned to the fluorinating agent NFSI and a multiplet at 157.8 ppm. The multiplet was assigned to fluorotrimethylsilane showing an interaction between NFSI and LiHMDS. This species has been previously been reported in the literature with a chemical shift of -159 ppm which is a slight deviation from the chemical shift seen in figure 3.11 however this signal can be assigned to fluorotrimethylsilane on the basis of its multiplicity.[63]

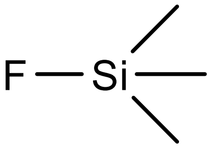

**Figure 3.12** Structure of fluorotrimethylsilane.

As expected, the $^{31}$P{$^1$H} spectra also showed no signals of significant interest with the main resonance being that for the protonated complex **4a** (87.9 ppm). Various signals were also observed in the range of 0-70 ppm. The spectrum was compared to that for the Milstein's hydroxo complex which was formed from the activation of water as it was assumed that formation of the protonated complex was due to water present in the system. No similarities could be drawn between the $^{31}P$ spectrum for Milstein's hydroxo complex and the spectrum obtained from the fluorination reaction.

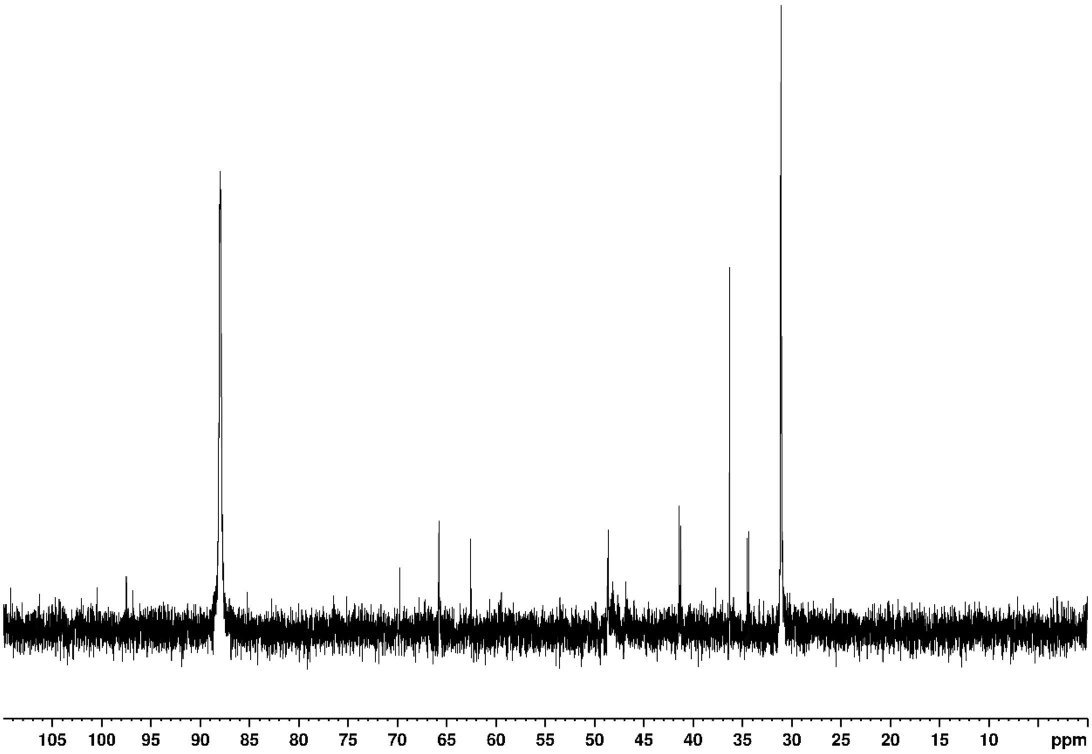

**Figure 3.13** $^{31}P\{^{1}H\}$ NMR spectra of product after addition of NFSI.

To optimise the reaction to prevent formation of the protonated complex and see formation of **5,** THF was used with a water content less than 10 ppm and the reaction was carried out at lower temperatures as this has previously shown success in favouring fluorination.[20]

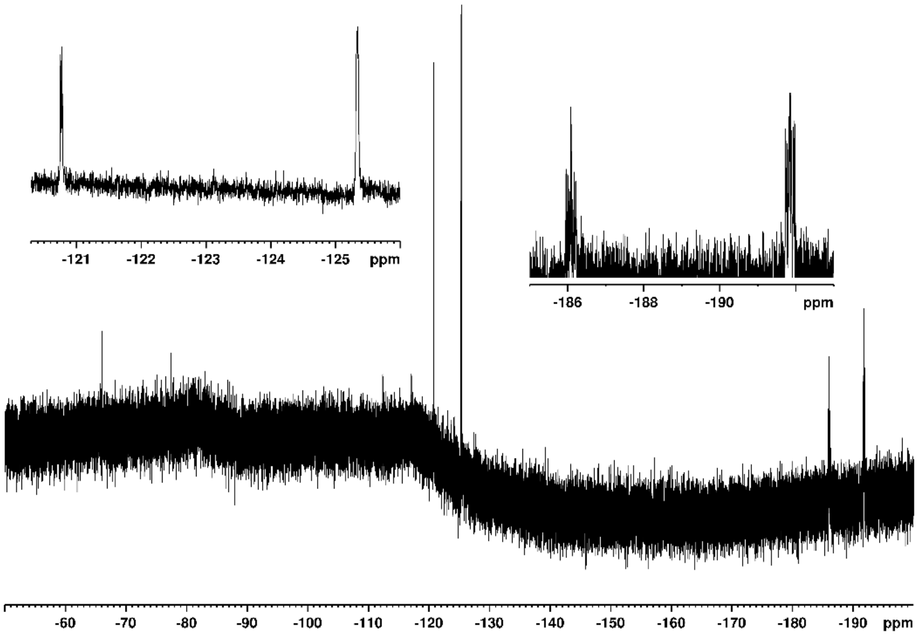

**Figure 3.14** $^{19}$F NMR of optimised fluorination reaction.

Figure 3.14 shows the formation of new fluorinated species not observed in previous reactions suggesting the presence of water was hindering the reaction also no signal is seen for the fluorotrimethylsilane. The ESI-MS showed formation of the protonated complex (m/z = 526.19) alongside evidence of fluorination (m/z = 544.18) and also the product of the addition of two fluorine atoms (m/z = 562.17). It was assumed that the mono-fluorination product in which the fluorine is added at the deprotonated benzylic arm, complex **5**, is responsible for the multiplets seen at -186 and -191.6 ppm (Figure 3.14) as noted in work carried out previously.[64] However, no evidence for the for the formation of the desired product, **5**, can be seen in the $^{31}$P{$^{1}$H} NMR spectrum (Figure 3.15). The reason for this could be due to a low concentration of **5** formed in the reaction and so the signals expected for **5** cannot be observed. Carrying out the reaction using a higher quantity of starting material (complex **4**) may resolve this issue. Due to the appearance of the signals no coupling data could be extracted however if the fluorine was added at the benzylic arm in the pincer ligand a value of approximately 30 Hz in the $^{19}$F{$^{1}$H} spectrum would be expected showing the fluorine is coupling to the phosphorus centre. The $^{31}$P{$^{1}$H} spectrum showed a singlet at 87.5 ppm which can be assigned to **4a** and no other resonances were observed. The position to which the fluorine attaches cannot be defined however as the NMR spectra correspond with previous unpublished work a tentative assignment can be given to fluorination of the benzylic arm to form **5.**[64]

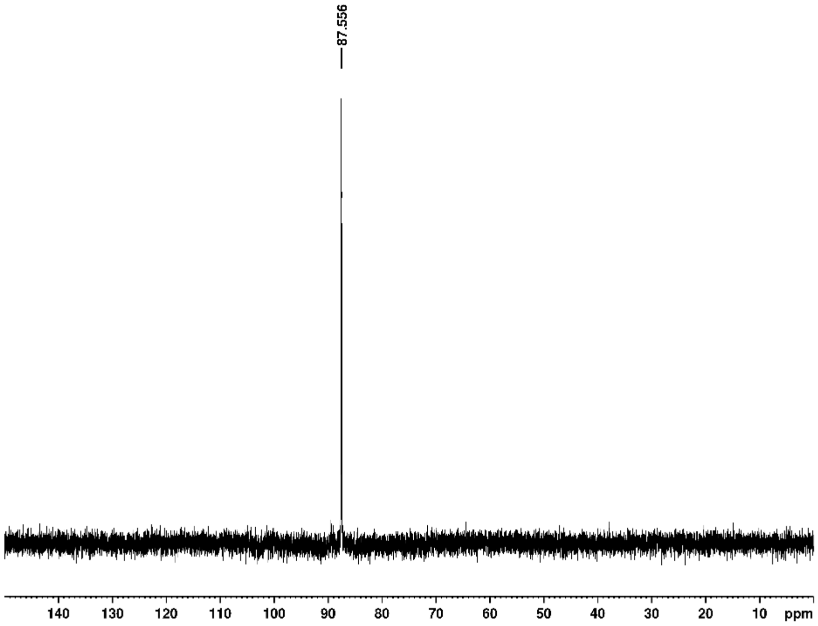

**Figure 3.15** $^{31}P\{^{1}H\}$ NMR spectrum of product for optimised fluorination reaction.

The ESI-MS data and the spectrum shown in figure 3.15 suggests there is competition between the formation **4a** and **5** however **4a** is favoured as this is seen as the major product. A doublet is seen at -120.7ppm with a coupling constant of *J* = 8.65 Hz and a singlet at 125.3 ppm which could potentially be a result of fluorination of the pyridine ring as a previously reported example in which the pyridine ring was disubstituted in the meta position gave a chemical shift of -125 ppm.[65]

### 3.2.3 Reaction with Umemoto's Reagent

Umemoto's reagent was used as an electrophilic source of a trifluoromethyl group. The reaction was carried out in a similar way as the fluorination reactions, LiHMDS in THF was added to a solution of **3** in THF and a colour change to yellow was observed indicating deprotonation. A colour change from yellow to green was previously described for this reaction as outlined previously (see page 49). One equivalent of

Umemoto reagent was immediately added and the solution concentrated under reduced pressure, a sample was taken and $^{31}P\{^1H\}$ and $^{19}F$ NMR spectra were recorded.

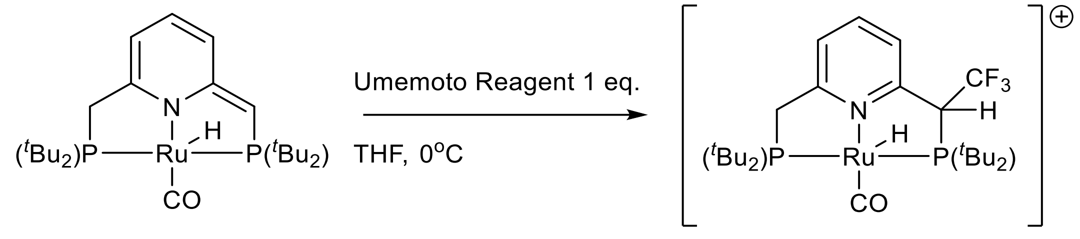

**4** **6**

**Scheme 3.7** Proposed synthesis of Trifluoromethylated complex (**6**)

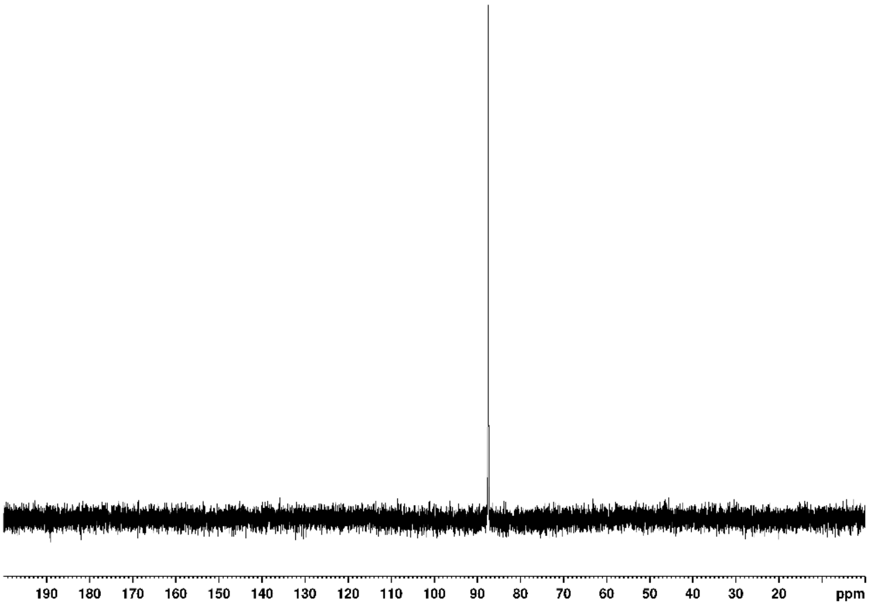

**Figure 3.16** $^{31}P\{^1H\}$ NMR spectrum of product after addition of Umemoto Reagent.

The NMR spectrum in figure 3.16 shows no evidence for the formation of **6** as only a single resonance is observed at 87.5 ppm which can be assigned to **4a**. However, the ESI-MS does show the presence of a product with a trifluoromethyl group (m/z = 594.18) added and unlike in the fluorination reaction no evidence of bis-trifluoromethylation, again the major product seen in the ESI-MS is **4a**. Upon addition of Umemoto reagent two new signals can now be seen in the $^{19}$F NMR spectrum.

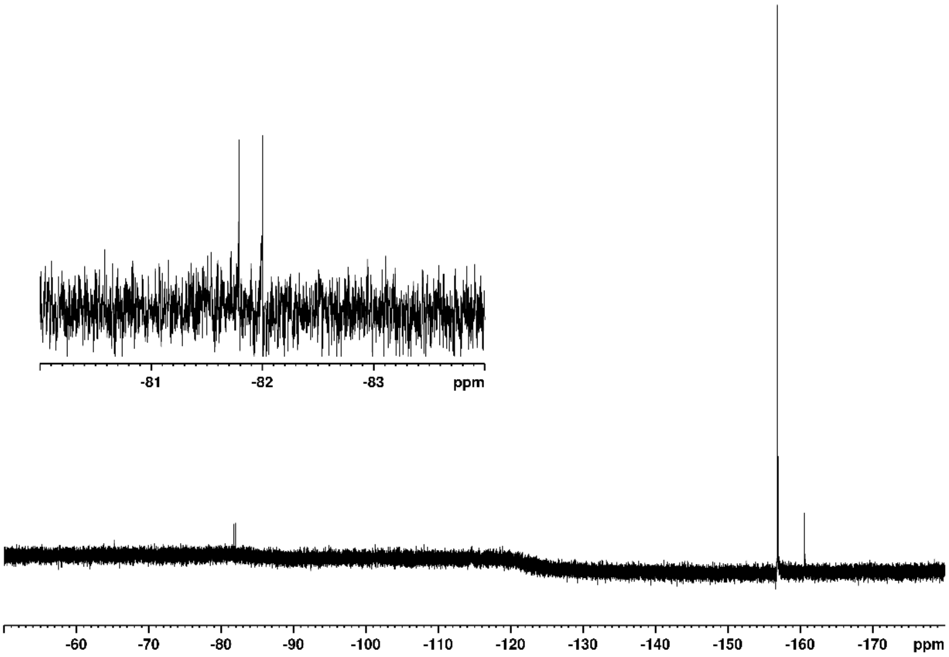

**Figure 3.17** $^{19}$F NMR spectrum after addition of Umemoto Reagent.

The $^{19}$F NMR spectrum shows a resonance at -156.9 ppm which can be assigned to the tetrafluoroborate anion and the resonance at -160.6 indicates the formation of fluorotrimethylsilane which was not observed for the fluorination reactions. The signals at approximately -80 ppm are of interest as these are within the expected range for a trifluoromethyl group. The identity of the signals is unclear as to whether it is a doublet or two singlets, if it is infact a doublet with a coupling of $J$ = 78.9 Hz then as no peaks with a similar coupling constant are seen in the $^{31}$P{$^{1}$H} NMR spectrum and no $^{1}$H NMR spectrum was collected due to running the NMR in protonated solvent then no atom can be assigned to which the group is coupling to. Due to the lack of information from the NMR spectra obtained and with no crystal structure of the product the position to which the $CF_3$ group is attached cannot be accurately determined.

### 3.2.4 Reaction with Bromoethane

Having investigated the addition of fluorine-containing electrophiles, bromoethane was selected as an electrophilic source of an alkyl group. The reaction was performed in the same manner as the fluorination and trifluoromethylations however for the addition of bromoethane one equivalent of AgOTf was added to improve the reactivity of the alkylating agent. $^{31}P\{^{1}H\}$ and $^{1}H$ NMR spectra were recorded of the solution using a $d_6$-benzene capillary to provide a lock.

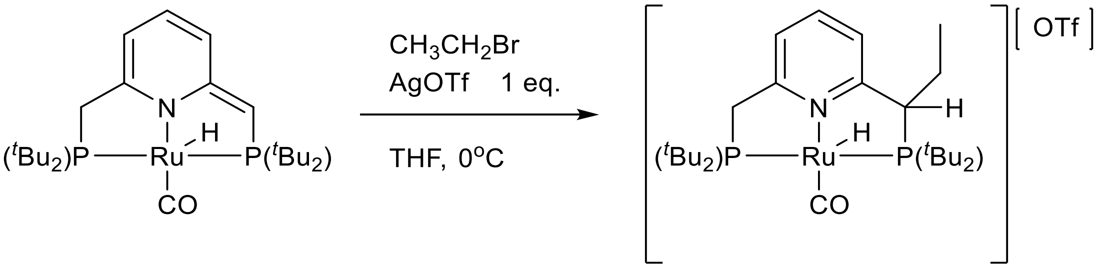

**4** **7**

**Scheme 3.8** Proposed synthesis of ethane substituted complex.

Along with the relevant NMR data an ESI-MS was also collected for the solution after addition of bromoethane and silver triflate and the results from this show no formation of **7** with the dominant product being the protonated complex **4a** (m/z = 526.19).

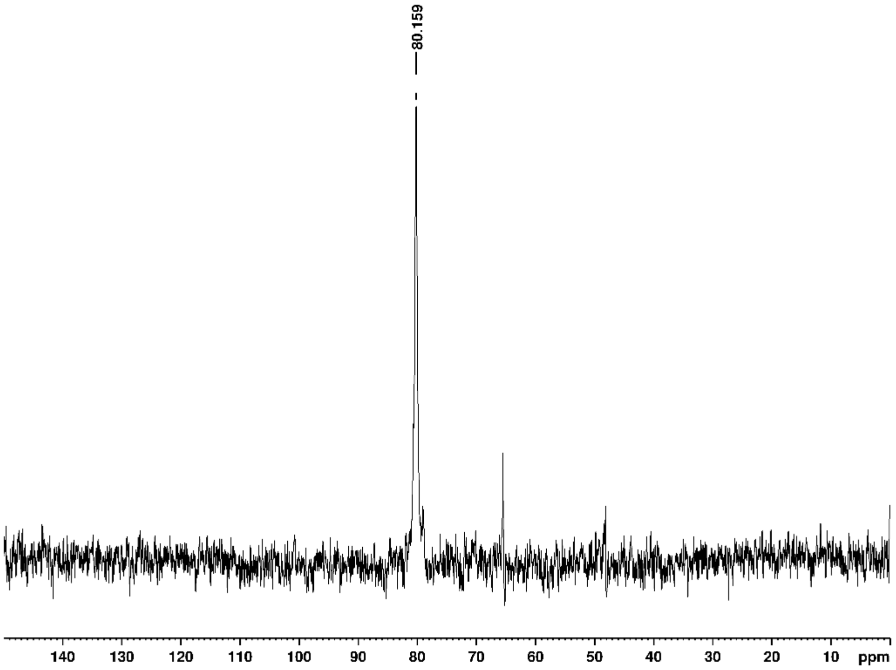

**Figure 3.18** $^{31}P\{^1H\}$ NMR spectrum of solution after bromoethane addition.

The spectrum in figure 3.18 displays a peak at 80.2 ppm which can be assigned to the protonated complex **4a** and as expected from the ESI-MS data no evidence for the formation of the desired product **7**. The singlet at 65.5 ppm could be an indication of an increase in moisture present in the system as this was previously seen in $^{31}P\{^1H\}$ spectra recorded for the initial fluorination reactions which were unsuccessful due to the presence of moisture.

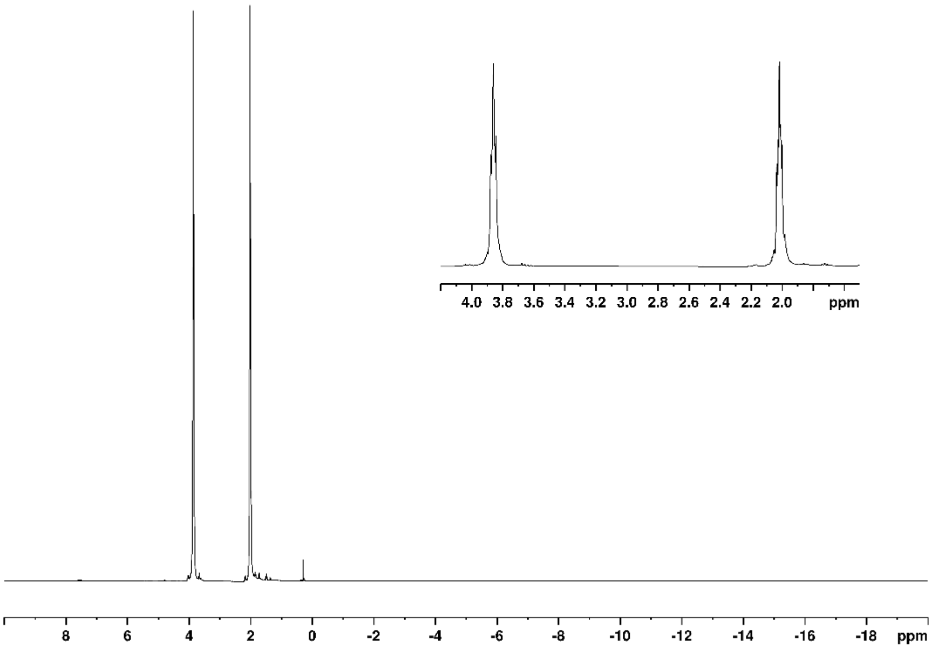

**Figure 3.19** $^1$H NMR spectrum after bromoethane addition.

The $^1$H spectrum is interesting as the the only resonances that are visible are two triplets at 3.86 ppm and 2.02 ppm which can be assigned to THF. All other resonances corresponding to the starting material, **4**, can no longer be seen such as the disappearance of the hydride signal at approximately -15 ppm.

### 3.2.5 Reaction with TMS-OTf

Trimethylsilyl triflate was used an electrophilic source of TMS and the reaction was carried out using a similar method as that for bromoethane however instead of AgOTf being used in this case CsF was used as an additive to increase the reactivity of the trimethylsilyl group by forming CsOTf.

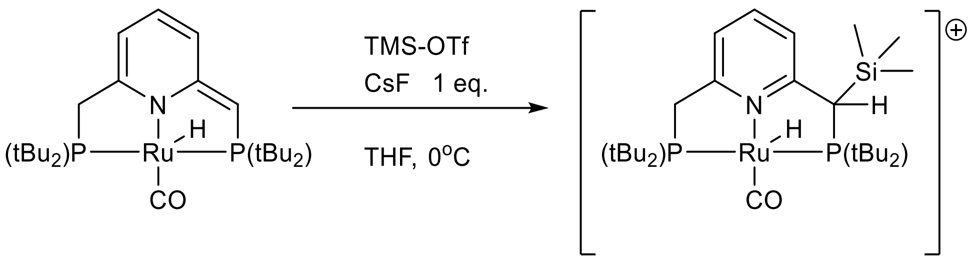

**4** **8**

**Scheme 3.9** Synthesis of TMS substituted complex.

Initial addition of TMS-OTf showed no colour change to the dearomatized complex solution however when CsF was added an immediate colur change was observed from dark green to yellow as seen in the fluorination and trifluoromethylation reactions. $^{31}$P{$^{1}$H} and $^{1}$H NMR were taken of the yellow solution alongside ESI-MS.

The ESI-MS showed formation of the protonated complex **4a** (m/z = 526.19) as the major product with no evidence for the presence of the desired species **8**. This is reflected in the $^{31}$P{$^{1}$H} NMR as shown in figure 3.20 as the signal for the protonated complex is observed at 89.4 ppm reinforcing the data from the ESI-MS that no conversion from **4** to complex **8** took place. Like with the $^{31}$P NMR for bromoethane shown in figure 3.18 a singlet is seen at 66.4 ppm and cannot be confidently assigned.

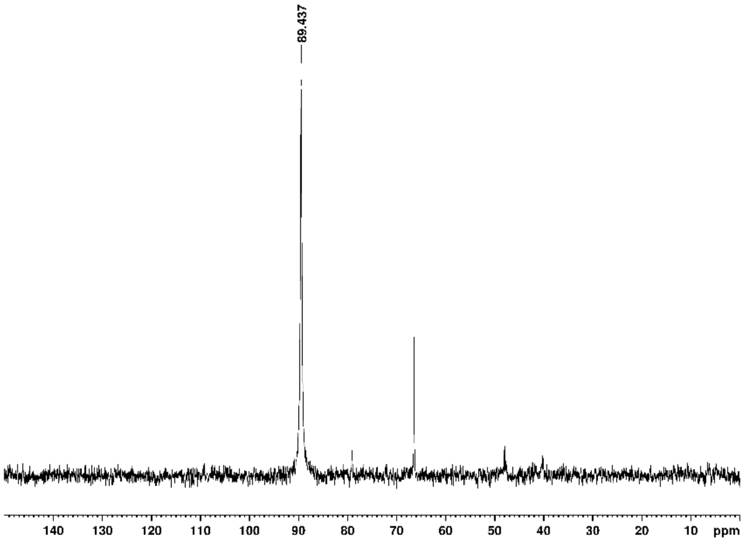

**Figure 3.20** $^{31}$P{$^{1}$H} NMR spectrum after addition of TMS-OTf to 4.

The $^1$H NMR spectrum shown in figure 3.21, like with the $^1$H NMR spectrum obtained for the bromoethane reaction (figure 3.19), shows only the resonances corresponding to THF with no others being visible to draw any conclusion from.

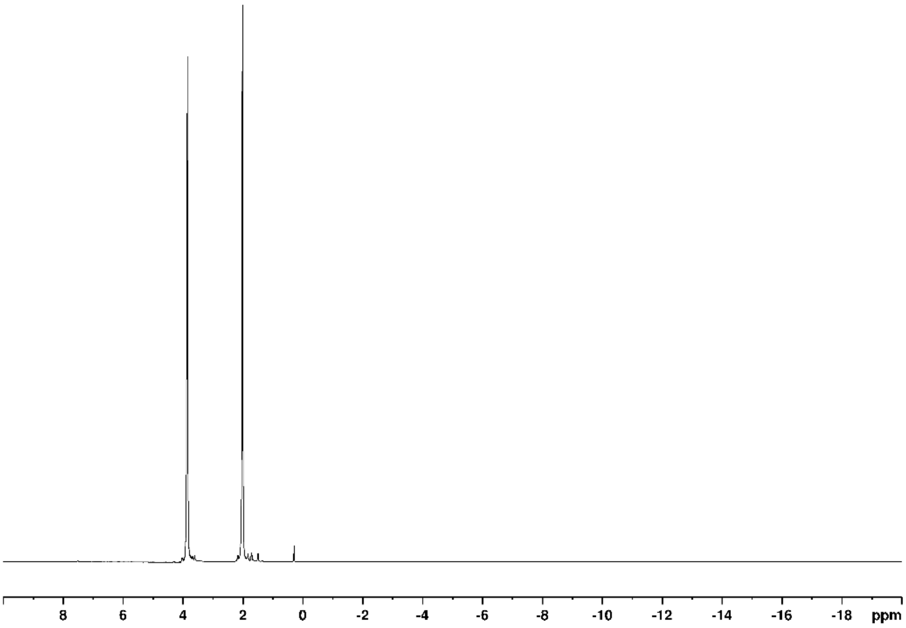

**Figure 3.21** $^1$H NMR spectrum taken after addition of TMS-OTf to 4.

This section therefore has demonstrated that addition of F and $CF_3$ into the complex structure is achievable based on ESI-MS and NMR data however the exact position to which the electrophile attaches cannot be confidently assigned. Further work is required for the synthesis of the alkyl substituted complexes as there was no evidence for the formation of **7** or **8**. This further work could include investigating different salts to help form the more reactive electrophile to drive the formation of the desired product. In all the reactions shown above the major product was the reprotonated complex, **4a,** indicating that protonation of the dearomatized complex is more facile. These findings are similar to those of previously unpublished material which concluded that although F and $CF_3$ addition was shown the exact position was unidentified and again the major product identified within the mass spec data was the reprotonated species.[64]

# 3.3 Computational Experiments

In order to build upon the synthetic work described above, computational experiments were carried out on a series of metal (Ru, Fe and Mg) pincer complexes bearing various fluorine-, carbon- and silicon-based electrophiles to further understand the effect of introducing electron donating/withdrawing groups into the ligand backbone and also to see the effect of electrophiles containing fluorine (F, $CF_3$) compared to those with hydrogens (H, $CH_3$,). Both the aromatized and dearomatized complexes were investigated. Geometry optimisations were carried out and from this key bond lengths and angles can be compared to those previously reported in the literature. Due to the presence of a metal carbonyl this allows for the electronic effect of these electrophiles on the metal centre to be studied through changes to the predicted vibrational modes. Reactivity studies were also carried out by assessing the ability of the dearomatized complex to act as a base with each electrophile in the ligand backbone compared with hydrogen. Optimised structures from which bond lengths and angles were measured were all calculated at the (RI-)BP86/SV(P) level. This methodology was selected as it has previously been applied to similar systems.[19]

## 3.3.1 Geometry Optimisations

### Ruthenium Pincer Complexes

Ruthenium pincer complexes have been heavily studied and so this provides a large library of structures to which the complexes investigated in this study can be compared. The lengths of metal-ligand bonds and the corresponding bond angles for each electrophile can be seen in table 3.1.

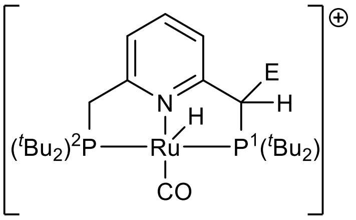

**9a**

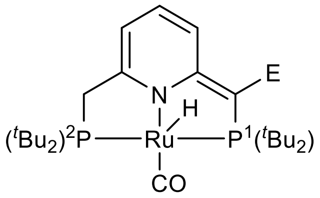

**9b**

E = H, F, $CF_3$, $CH_3$, $SiH_3$, $^t$Bu, TMS

**Figure 3.22** Structures of Ru pincer complexes investigated.

**9a**

| | Bond Length (Å) | | | |
|---|---|---|---|---|
| **Electrophile (E)** | **Ru-H** | **Ru-P1** | **Ru-P2** | **Ru-N** |
| **H** | 1.563 | 2.365 | 2.360 | 2.174 |
| **F** | 1.562 | 2.367 | 2.361 | 2.168 |
| **$CF_3$** | 1.563 | 2.359 | 2.372 | 2.161 |
| **$CH_3$** | 1.566 | 2.359 | 2.374 | 2.167 |
| **$SiH_3$** | 1.565 | 2.357 | 2.374 | 2.164 |
| **$^t$Bu** | 1.562 | 2.370 | 2.377 | 2.168 |
| **TMS** | 1.564 | 2.358 | 2.376 | 2.164 |

**9b**

| | Bond Length (Å) | | | |
|---|---|---|---|---|
| **Electrophile (E)** | **Ru-H** | **Ru-P1** | **Ru-P2** | **Ru-N** |
| **-** | 1.566 | 2.374 | 2.348 | 2.155 |
| **F** | 1.566 | 2.378 | 2.348 | 2.153 |
| **$CF_3$** | 1.567 | 2.378 | 2.348 | 2.150 |
| **$CH_3$** | 1.567 | 2.372 | 2.347 | 2.148 |
| **$SiH_3$** | 1.567 | 2.373 | 2.350 | 2.150 |
| **$^t$Bu** | 1.568 | 2.392 | 2.342 | 2.132 |
| **TMS** | 1.568 | 2.376 | 2.346 | 2.138 |

**Table 3.1** Metal-ligand bond lengths for Ru($^{tBu}$PNP) complexes calculated at the BP86 level of theory.

As shown in table 3.1 no significant effect is seen on the length of the metal—hydride bond with the introduction of a group into the ligand backbone with all reported values between 1.562 Å and 1.566 Å. A slight increase in the Ru-H bond length for the dearomatized complex is seen however this is only an increase of 0.002 Å – 0.006 Å. Previously reported ruthenium pincer complexes bearing a hydride ligand gave bond lengths in the region of 1.5 – 1.6 Å which the values shown in the table above are in agreement with. However, the PONOP complex in which the $-CH_2-$ groups in the ligand backbone are replaced with ether -O- atoms shows an increase in the Ru-H bond length to 1.72 Å.[25,30,33,38] The Ru-P bond lengths (P1 phosphine is that bonded to the carbon to which the electrophile attaches) particularly the P1 bond length, show only minimal changes with the introduction of a group into the ligand backbone in a similar manner to the hydride bond. In the aromatized complexes the **F** and **H** substituted complexes gave Ru-P1 bond lengths of 2.367 Å and 2.365 Å respectively and a reduction in length is seen for the remaining groups with **9a-$^t$Bu** being the exception. This increase in Ru-P1 bond length is also seen in the dearomatized complex. In **9a** as, bulkier substituents are introduced into the ligand backbone the length of the Ru-P2 bond can be seen to increase in length (**9a-H** = 2.360 Å, **9a-CF$_3$** = 2.372 Å and **9a-$^t$Bu** = 2.377 Å). This increase in the length of the Ru-P2 bond could be due to the increased steric bulk around the metal centre as the groups in the ligand backbone causes rearrangement of the tert-butyl groups closer to the metal centre.

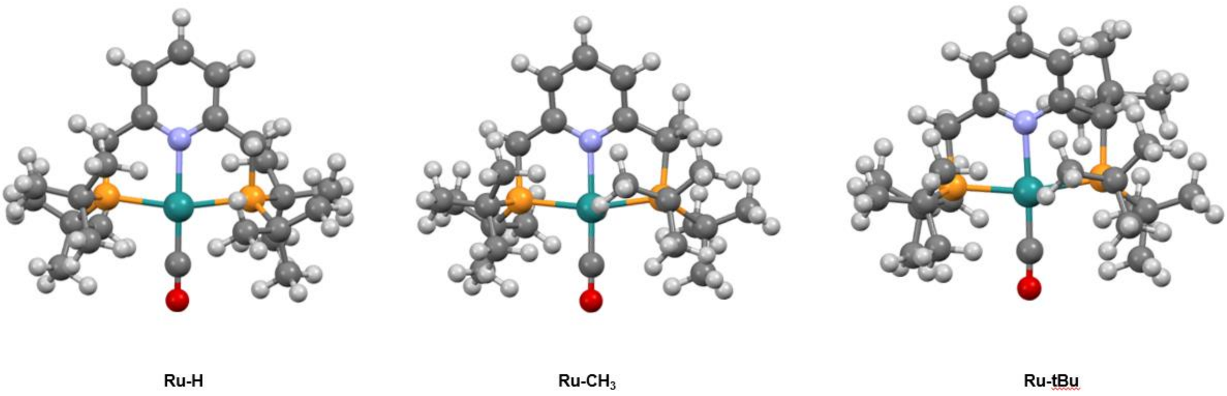

Ru-H

Ru-CH$_3$

Ru-tBu

**Figure 3.23** Structures of ruthenium complexes showing increased steric bulk around the metal centre.

This increase in the length of the Ru-P2 bond is not observed for the dearomatized ruthenium complexes as all the bond lengths sit between 2.342 Å and 2.350 Å. This could be due to a reduced steric influence of the P1 tert butyl groups as little rearrangement is required to accommodate the substituted electrophile in the ligand backbone.

Bond angles around the metal centre were also measured to see if any change in geometry is seen when an electrophile is introduced into the system.

| | **9a** | | | | **9b** | | |
|---|---|---|---|---|---|---|---|
| | **Bond Angle (°)** | | | | **Bond Angle (°)** | | |
| **Electrophile (E)** | **P2-Ru-P1** | **N-Ru-CO** | **N-Ru-H** | **Electrophile (E)** | **P2-Ru-P1** | **N-Ru-CO** | **N-Ru-H** |
| **H** | 165.33 | 176.50 | 89.85 | **-** | 163.93 | 178.83 | 91.46 |
| **F** | 165.69 | 176.39 | 89.63 | **F** | 164.56 | 178.64 | 91.23 |
| **$CF_3$** | 167.16 | 176.90 | 95.09 | **$CF_3$** | 165.19 | 177.45 | 89.87 |
| **$CH_3$** | 166.10 | 179.07 | 93.33 | **$CH_3$** | 164.03 | 178.44 | 90.77 |
| **$SiH_3$** | 166.20 | 179.10 | 93.37 | **$SiH_3$** | 164.36 | 178.19 | 90.55 |
| **$^t$Bu** | 165.41 | 176.92 | 95.89 | **$^t$Bu** | 165.02 | 176.92 | 89.62 |
| **TMS** | 165.41 | 178.75 | 94.26 | **TMS** | 164.57 | 178.09 | 90.45 |

**Table 3.2** Metal-ligand bond angles.

The optimised structures obtained (examples shown in figure 3.23) for both the aromatized and dearomatized complexes show they adopt a distorted square pyramidal geometry in which the -CO ligand is *trans* to the pyridine nitrogen, demonstrated by the N-Ru-CO bond angles in table 3 with near linear values. The hydride ligand is *cis* to the pyridine nitrogen with bond N-Ru-H bond angles being between 89°-95° and 89°-91° for the aromatized and dearomatized complexes respectively

### Iron Pincer Complexes

To further expand this work, the effect of changing the metal centre on metal-ligand bond lengths/angles was investigated. Iron was selected as it lies in the same group as ruthenium and so no changes to the coordinating ligands are required and there are a variety of examples of iron pincer complexes that can be found within the literature which allows for comparisons to be drawn between this work and that previously reported (spin unrestricted calculations were used for the iron complexes).

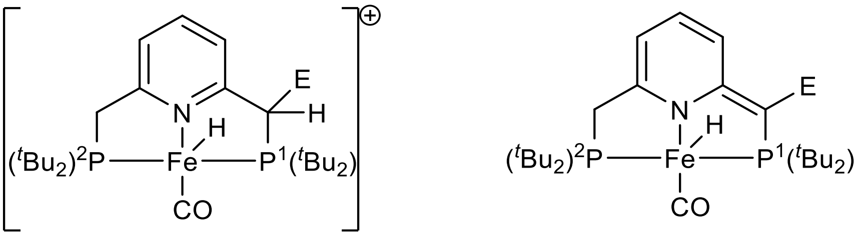

**10a** **10b**

E = H, F, $CF_3$, $CH_3$, $SiH_3$, $^t$Bu, TMS

**Figure 3.24** Iron Pincer complexes investigated. E denotes the electrophilic group added.

**10a**

| Electrophile (E) | Bond Length (Å)<br>Fe-H | Fe-P1 | Fe-P2 | Fe-N |
|---|---|---|---|---|
| **H** | 1.473 | 2.242 | 2.234 | 2.029 |
| **F** | 1.472 | 2.244 | 2.236 | 2.019 |
| **$CF_3$** | 1.472 | 2.226 | 2.256 | 2.015 |
| **$CH_3$** | 1.476 | 2.229 | 2.254 | 2.022 |
| **$SiH_3$** | 1.475 | 2.225 | 2.254 | 2.016 |
| **$^t$Bu** | 1.472 | 2.238 | 2.259 | 2.021 |
| **TMS** | 1.473 | 2.226 | 2.256 | 2.018 |

**10b**

| Electrophile (E) | Bond Length (Å)<br>Fe-H | Fe-P1 | Fe-P2 | Fe-N |
|---|---|---|---|---|
| **H** | 1.477 | 2.254 | 2.216 | 2.009 |
| **F** | 1.477 | 2.257 | 2.218 | 2.004 |
| **$CF_3$** | 1.476 | 2.261 | 2.220 | 2.007 |
| **$CH_3$** | 1.478 | 2.254 | 2.217 | 2.000 |
| **$SiH_3$** | 1.477 | 2.254 | 2.219 | 2.004 |
| **$^t$Bu** | 1.477 | 2.269 | 2.218 | 1.993 |
| **TMS** | 1.477 | 2.256 | 2.218 | 1.993 |

**Table 3.3** Metal-ligand bond lengths for the optimised structures of Iron pincer complexes.

Table 3.3 shows the metal-ligand bond lengths for a series of Iron pincer complexes with various electrophiles in the ligand backbone. The data for the Fe-H bond length shows that changing the nature of the electrophile added into the ligand backbone has a minimal effect as the bond length shows little deviation, a trend that was also seen for the ruthenium pincer complexes investigated. For example, in **10a** the Fe-H bond length is in the range of 1.472 – 1.476 Å and for **10b** 1.476 – 1.478 Å. Previously reported Iron pincer complexes with a hydride bound to the metal centre report a consistent Fe-H bond length of 1.42 Å.[31,56,66] The complexes in this study show slight elongation of the Fe-H bond compared to those previously reported In the literature with no substituent added at the $\alpha$-carbon relative to the phosphine atom. The Fe-P bond lengths follow a similar trend to that seen for the ruthenium complexes in that for the aromatized iron complexes the H and F substituted complexes gave similar Fe-P1 bond lengths with values of 2.242 Å and 2.244 Å respectively, for the remaining complexes all Fe-P1 lengths were within the range of 2.225 Å – 2.229 Å excluding the *ᵗ*Bu substituted complex which again gave an elongated bond at 2.238 Å. Also, as with the ruthenium the species, the iron complexes show that with the introduction of bulkier substituents into the ligand backbone an elongation of Fe-P2 bond is observed owing to steric hindrance between the tert-butyl groups of the two phosphine centres. Previously reported iron pincer complexes gave Fe-P bond lengths in the range of 2.17 Å – 2.24 Å which the values shown in table 3 are in good agreement with.[32,55,56]

As with the ruthenium pincer complexes the iron species also adopt a distorted square pyramidal geometry with the -CO ligand *trans* to the pyridyl nitrogen and the hydride *cis*, this is reflected in the bond angles shown in the table below. Like with the analogous ruthenium complexes, table 3.4 shows that the metal-ligand bond angles in **10a/10b** show little change with the introduction of each electrophile. Examples of previously reported iron pincer complexes within the literature gave sub-linear P-Fe-P bond angles with values of 163.75°[56], 164.46°[67] and 167.59°[44]. These bond angles show a slight reduction compared with those in table 3.4. The N-Fe-CO bond angles are within the range of 174.63° - 178.88° in **10a** and 175.80°-179.10° in **10b**. These values are in agreement with those found in the literature (175.79°[61], 179.44°[60]).

| | 10a | | | | 10b | | |
|---|---|---|---|---|---|---|---|
| | Bond Angle (°) | | | | Bond Angle (°) | | |
| **Electrophile (E)** | **P2-Fe-P1** | **N-Fe-CO** | **N-Fe-H** | **Electrophile (E)** | **P2-Fe-P1** | **N-Fe-CO** | **N-Fe-H** |
| **H** | 170.84 | 174.63 | 90.12 | **-** | 169.78 | 178.59 | 92.68 |
| **F** | 171.01 | 175.27 | 90.35 | **F** | 170.49 | 179.10 | 93.10 |
| **$CF_3$** | 172.64 | 177.50 | 94.74 | **$CF_3$** | 170.77 | 176.89 | 90.75 |
| **$CH_3$** | 171.87 | 177.50 | 92.17 | **$CH_3$** | 169.76 | 178.34 | 92.12 |
| **$SiH_3$** | 171.99 | 177.96 | 92.67 | **$SiH_3$** | 170.07 | 177.80 | 91.62 |
| **$^t$Bu** | 171.09 | 177.98 | 95.32 | **$^t$Bu** | 170.29 | 175.80 | 89.65 |
| **TMS** | 171.29 | 178.88 | 93.84 | **TMS** | 170.17 | 177.87 | 91.50 |

**Table 3.4** Metal-ligand bond angles for Fe pincer complexes.

## Magnesium Pincer Complexes

As transition metals (Fe and Ru) have been investigated, the metal centre was changed to a non-transition metal, in this case magnesium, to determine what differences are observed in the structure of the resulting complexes. However, no examples of previously synthesised and characterised magnesium pincer complexes can be found within the literature which means no comparisons can be made. Table 3.5 shows the measured metal-ligand bond lengths for the investigated complexes.

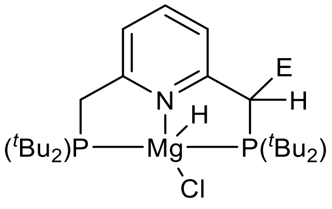

**11a**

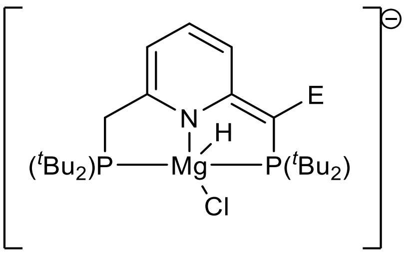

**11b**

E = H, F, $CF_3$, $CH_3$, $SiH_3$, $^t$Bu
and TMS

**Figure 3.25** Structure of Magnesium pincer complexes investigated.

|  | 11a |  |  |  |  | 11b |  |  |  |
|---|---|---|---|---|---|---|---|---|---|
|  | Bond Length (Å) |  |  |  |  | Bond Length (Å) |  |  |  |
| **Electrophile (E)** | **Mg-H** | **Mg-P1** | **Mg-P2** | **Mg-N** | **Electrophile (E)** | **Mg-H** | **Mg-P1** | **Mg-P2** | **Mg-N** |
| **H** | 1.777 | 2.694 | 2.696 | 2.494 | **-** | 1.808 | 2.686 | 2.742 | 2.326 |
| **F** | 1.774 | 2.718 | 2.695 | 2.493 | **F** | 1.803 | 2.738 | 2.772 | 2.274 |
| **$CF_3$** | 1.766 | 2.746 | 2.773 | 2.475 | **$CF_3$** | 1.794 | 2.640 | 2.744 | 2.330 |
| **$CH_3$** | 1.773 | 2.714 | 2.755 | 2.508 | **$CH_3$** | 1.807 | 2.659 | 2.740 | 2.310 |
| **$SiH_3$** | 1.770 | 2.725 | 2.757 | 2.500 | **$SiH_3$** | 1.804 | 2.661 | 2.741 | 2.322 |
| **$^t$Bu** | 1.770 | 2.709 | 2.772 | 2.460 | **$^t$Bu** | 1.794 | 2.678 | 2.897 | 2.220 |
| **TMS** | 1.772 | 2.710 | 2.763 | 2.488 | **TMS** | 1.807 | 2.668 | 2.756 | 2.295 |

**Table 3.5** Measured metal-ligand bond lengths for Mg pincer complexes.

As previously seen with both the iron and ruthenium complexes the Mg-H bond shows minimal change in the aromatized complex with the introduction of an electrophile with reported values, excluding **11a-$CF_3$**, in the range of 1.770 – 1.777 Å. This difference in bond lengths in **11a-$CF_3$** is odd as for both the iron and ruthenium species no significant change of the M-H bond length was observed upon changing the electrophile within the backbone. The same applies for the Mg-P1 bond. This difference is difficult to rationalise as it is unlikely due to steric effects as this has been shown to have a minimal impact for bulkier electrophiles in all complexes investigated. The same trend is observed also for the dearomatized complex however a slight elongation of the Mg-H bond is seen with the majority of values in the range of 1.803 – 1.808 Å with the exception of **11b-$CF_3$** and **11b-$^t$Bu** which both gave the Mg-H bond length of 1.794 Å. A significant difference with the magnesium complexes compared with the iron and ruthenium species is the elongation of the Mg-P bonds by approximately 0.5 Å indicating the reduced donor ability of phosphorus to magnesium compared with ruthenium and iron. The Mg-P2 bond length follows the same trend as observed for Ru and Fe which is that as bulkier substituents are introduced into the ligand backbone the length of the Mg-P2 bond increases (**11a-H** = 2.696 Å, **11a-$CH_3$** = 2.755 Å, **11a-$^t$Bu** = 2.772 Å). The Mg-P1 bond lengths in both the iron and ruthenium complexes above showed minimal change with each electrophile however in the corresponding magnesium complexes the Mg-P1 varies for each electrophile with no discernible trend for both the aromatized and dearomatized species.

While the Ru and Fe based-pincer complexes adopted a distorted square pyramidal geometry, the magnesium complexes are arranged in a trigonal bipyramidal geometry as shown in the figure below. A noticeable difference in the magnesium complexes is that the chloride ligand is *cis* to the pyridine nitrogen compared to the *trans* carbonyl and this is shown in table 6 as the N-Mg-Cl show a significant reduction in linearity and also the change in electrophile appears to have a significant effect on not only this angle but the other metal-ligand bond angles also. For example, the N-Mg-Cl bond angle in the aromatized complex gave values of 141.55° and 141.28° for the H and F substituted complexes respectively showing a large difference from the expected 120° with the remaining complexes in the range of 112.16°-124.37°. The P-Mg-P bond angle also shows deviation away from the near linear values obtained for the iron and ruthenium complexes with values in the region of 130°-160° and each electrophile investigated appears to impact this bond angle which was not observed for iron and ruthenium.

| | **11a** | | | | **11b** | | |
|---|---|---|---|---|---|---|---|
| | **Bond Angle (°)** | | | | **Bond Angle (°)** | | |
| **Electrophile (E)** | **P2-Mg-P1** | **N-Mg-Cl** | **N-Mg-H** | **Electrophile (E)** | **P2-Mg-P1** | **N-Mg-Cl** | **N-Mg-H** |
| **H** | 138.71 | 141.55 | 90.44 | **-** | 149.81 | 128.40 | 109.33 |
| **F** | 139.25 | 141.28 | 90.09 | **F** | 152.32 | 121.43 | 114.13 |
| **$CF_3$** | 151.48 | 112.16 | 117.72 | **$CF_3$** | 141.21 | 140.61 | 99.29 |
| **$CH_3$** | 145.47 | 124.37 | 106.82 | **$CH_3$** | 149.15 | 130.54 | 107.45 |
| **$SiH_3$** | 146.58 | 122.94 | 108.96 | **$SiH_3$** | 149.15 | 130.51 | 106.73 |
| **$^t$Bu** | 149.57 | 119.40 | 113.82 | **$^t$Bu** | 156.62 | 120.79 | 110.03 |
| **TMS** | 147.14 | 122.43 | 110.78 | **TMS** | 151.50 | 128.37 | 107.36 |

**Table 3.6** Measured metal-ligand bond angles for Mg pincer complexes.

In summary the optimised structures detailed in this section appear to show that by introducing a new group into the ligand backbone a minimal effect on the metal-ligand bond lengths is seen along with no change in the geometry of the complex. However, when the nature of the metal centre is changed from a transition metal (Ru, Fe) to a group II metal (magnesium) the structures show elongated metal-ligand bond lengths and a significantly distorted geometry.

## 3.3.2 Carbonyl Stretching Frequency

As both the ruthenium and iron species shown previously contain a metal-carbonyl bond this allows for the calculated stretching frequency of the carbonyl to be used as a probe for the electron density of the metal centre. The carbonyl-metal bond can undergo back-bonding due to the carbonyl carbon possessing low lying orbitals of π symmetry which allows for an interaction with filled metal d-orbitals. This process relies largely on the electron density of the metal atom and so the carbonyl stretching frequency is a good indication of the effect that introducing substituents into the ligand backbone has on the electronic properties of the metal. A reduction in $v_{CO}$ for example would suggest an increase in back-bonding which results in population of the antibonding CO orbital and so the CO bond order is reduced giving a lower stretching frequency and the opposite is true if an increase in $v_{CO}$ is observed. Due to the geometry the pincer complexes studied adopt the CO ligand is placed trans to the pyridine nitrogen and so the trans effect between these two ligands will also have an impact on the CO stretching frequency. Figure 3.26 shows the calculated CO stretching frequency of **10a/b** for all electrophiles.

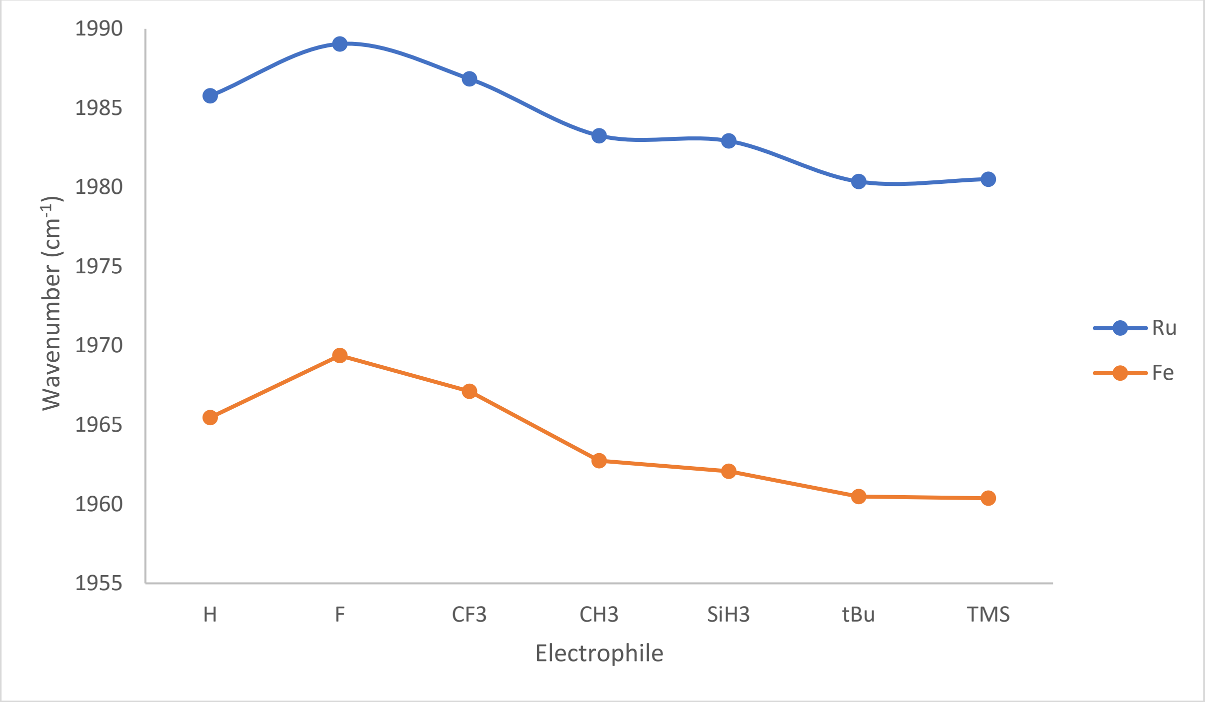

**Figure 3.26** Graph showing the calculated $\nu_{CO}$ for the aromatized Fe and Ru pincer complexes.

The graph in figure 3.26 shows that no significant change is seen in the $\nu_{CO}$ upon changing the electrophile within the ligand backbone (**9a/10a** all carbonyl stretching frequencies are within a 10 cm$^{-1}$ window (**9a** = 1980 – 1990 cm$^{-1}$, **10a** = 1960 – 1970 cm$^{-1}$). However, figure 3.26 does show that the complexes containing electrophiles that are more electron-donating in nature reported a reduced $\nu_{CO}$ value compared with those bearing substituents that are more electron-withdrawing. As can be observed in figure 3.26 when F and $CF_3$ are added into the ligand backbone a slight increase is seen compared to the value for H and then with the introduction of $CH_3$ and $SiH_3$ the $\nu_{CO}$ value decreases and with $^t$Bu and TMS a further reduction is seen (Figure 3.27), this can be applied to both the ruthenium and iron species.

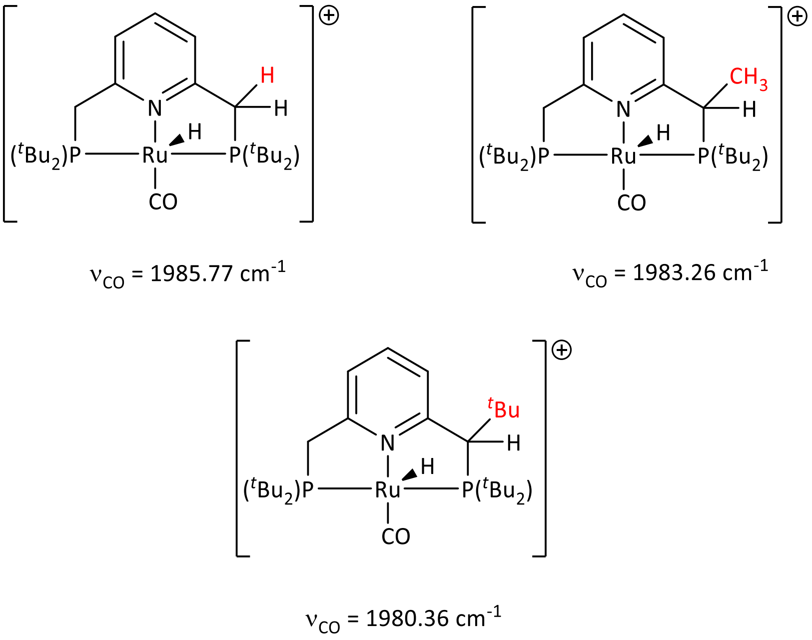

**Figure 3.27** Ru pincer complexes with electrophile added in backbone and corresponding CO stretching frequency.

Examples within the literature show that by changing the linker atom a shift in the reported $\nu_{CO}$ values is observed. For example, a Ru($^{iPr}$PNP) complex gave a stretching frequency of 1903 cm$^{-1}$, however, when the $-CH_2-$ groups within the ligand backbone are replaced with ether -O- atoms to give the PONOP complex the measured stretching frequency increases to 1932 cm$^{-1}$. This indicates that π back-bonding is reduced in the PONOP complex compared with the analogous PNP.[38] Previously reported Ru and Fe pincer complexes also display a significant difference between the reported $\nu_{CO}$ values with the Fe complexes giving lower stretching frequencies as observed in this work.[23,33,38,52,55,56] The measured metal-carbon bond lengths can also give some insight into the extent of back-bonding between the metal and carbonyl carbon and hence the CO stretching frequency. The metal-carbon bond lengths show minimal change with the addition of each electrophile as the data shown in figure 3.26 would suggest as only small changes are seen in for the CO stretching frequency values. In the ruthenium species all M-C bond lengths are within the range of 1.848 – 1.854 Å with the shorter bond lengths assigned to **9a-$^t$Bu** and **9a-TMS** and the longest bond length can be assigned to **9a-F** which corresponds with the data in figure 3.26.

The iron pincer complexes report a reduction in CO stretching frequency for all electrophiles by approximately 20 cm$^{-1}$ with all stretching frequencies between 1960 cm$^{-1}$ and 1970 cm$^{-1}$. This reduction in wavenumber would suggest that back-bonding between Fe and **C**O is greater than between Ru and **C**O. This is reflected in the measured Fe-carbon bond lengths which too show a reduction in length compared to the ruthenium species with all Fe-C bond lengths within the range 1.724 – 1.272Å showing a reduction of approximately 0.1 Å for each electrophile. A reason for this could be Fe(II) is smaller than Ru(II). As outlined above the shorter M-C bond length for the Iron species may indicate an increase in back-bonding which in-turn weakens the CO bond and so a reduction in stretching frequency is observed. Like with the ruthenium species when electrophile was added into the backbone that is more electron-donating in nature a reduction in $\nu_{CO}$ was seen (**10a-H** = 1965.47 cm$^{-1}$, **10a-CH$_3$** = 1962.73 cm$^{-1}$, **10a-TMS** = 1960.37 cm$^{-1}$).

The carbonyl stretching frequency for the dearomatized complexes (**9b/10b**) were also calculated and can be seen in figure 3.28.

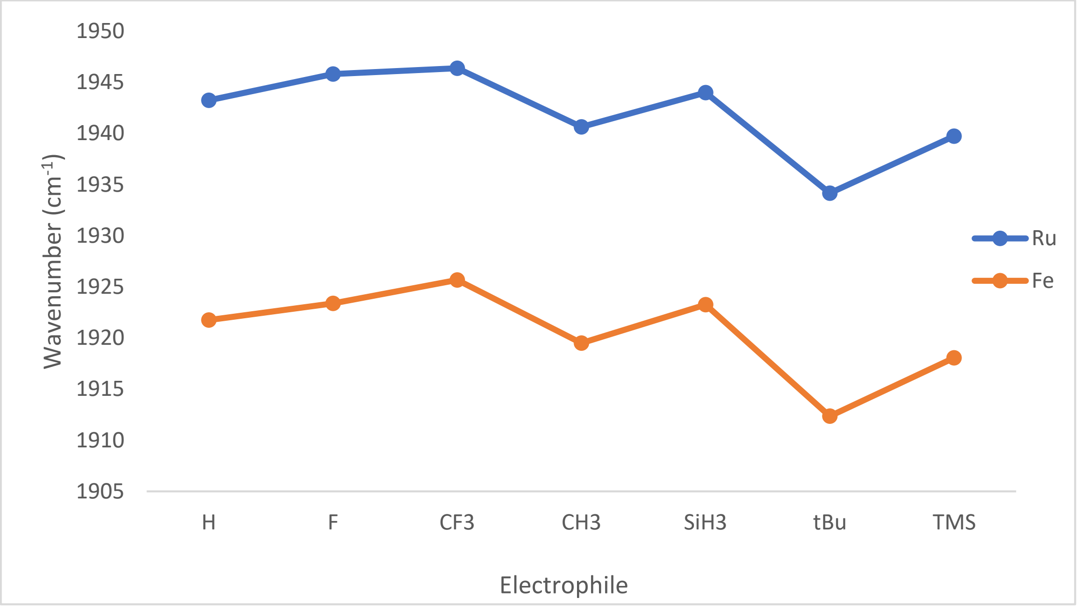

**Figure 3.28** Graph showing calculated $\nu_{CO}$ values for the dearomatized Ru/Fe pincer complexes.

Figure 3.28 shows that the dearomatized complexes (**9b/10b**) gave significantly reduced wavenumbers (approximately 40 cm$^{-1}$) for both metal centres with the ruthenium values now between 1934 – 1946 cm$^{-1}$ and iron 1912 – 1925 cm$^{-1}$. This reduction would suggest that in the dearomatized complex the electron density of the metal centre is greater meaning increased back-bonding. This is evidenced by the measured M-C bond lengths which show a slight reduction. The reduction in stretching frequency could also be due to the reduction in charge of the dearomatized complexes (neutral) compared to the aromatized counterparts (cationic). The CO stretching frequency is reduced in the neutral dearomatized complex compared with the cationic aromatized complex as back donation is increased due to stronger overlap between the metal and carbon orbitals which results in a lower stretching frequency.

The CO stretching frequency for both the ruthenium and iron species shows an increase for F and $CF_3$ compared with H. For example, **9b-H** gave a stretching frequency of 1943.23 cm$^{-1}$, in **9b-F** this value was 1945.79 cm$^{-1}$ and then in **9b-CF$_3$** a further increase is seen to 1946.37 cm$^{-1}$. A reason for this observed change could be that the substituents have an influence on the donor ability of the P1 atom to the metal centre which would affect the electron density of the metal centre. However, as shown in table 3.1 and 3.3 no significant change in the length of M-P1 bond is seen and the subtle differences do not correlate with the changes in CO stretching frequency. In the dearomatized complexes unlike in the aromatized complexes when silicon-based electrophiles are added to the ligand backbone an increase in stretching frequency is observed compared to the carbon electrophiles. **9b-CH$_3$** gave a CO stretching frequency of 1940.62 cm$^{-1}$ and **9b-SiH$_3$** 1943.98 cm$^{-1}$. A similar change is seen in the iron complex as **10b-CH$_3$** gave a CO stretching frequency of 1919.48 cm$^{-1}$ and **10b-SiH$_3$** 1923.24 cm$^{-1}$ showing an increase albeit by only approximately 4 cm$^{-1}$. This change in the dearomatized complexes could be due to the increased donor ability of the pyridyl nitrogen to the central metal compared with the aromatized complexes and in the silicon substituted species this donor ability is reduced compared the carbon based electrophiles resulting in an increase in stretching frequency. This increase can also be seen between the $^t$Bu and TMS species. In the aromatized species however $CH_3$/$SiH_3$ and $^t$Bu/TMS both gave similar stretching frequencies.

## 3.3.3 Isodesmic Calculations

In order to probe the reactivity of the pincer complexes bearing different electrophiles in the ligand backbone further an isodesmic reaction (figure 21) was used to assess the ability of the dearomatized complex to act as a base and to determine how each electrophile affects this ability and also what affect if any changing the metal centre has.

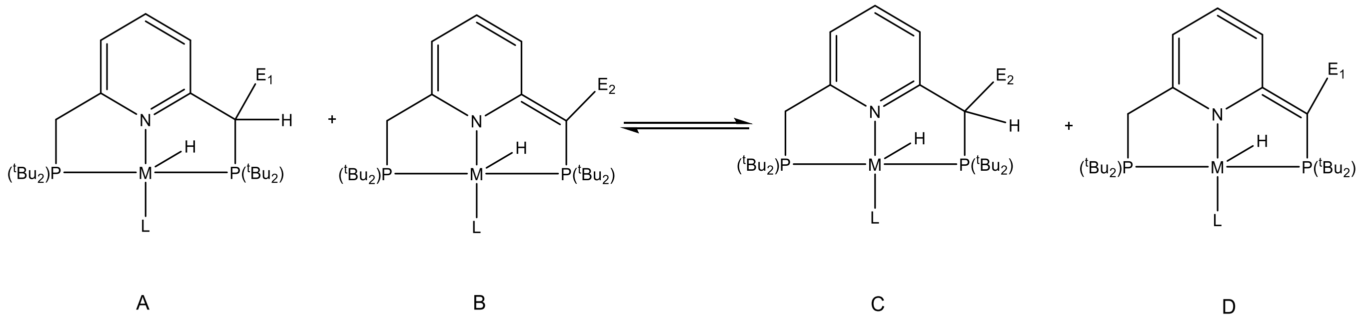

M = Ru,Fe ; L = CO
Mg ; L = Cl

E1 = H
E2 = H, F, $CF_3$, $CH_3$, $SiH_3$, tBu, TMS

**Figure 3.29** Isodesmic reaction used for reactivity studies.

As shown in figure 3.29 the ability of **B** to act as a base to form the aromatized complex **C** was investigated and the energy change associated with this transformation ($\Delta$G) was calculated for each metal centre (Ru/Fe/Mg) and all electrophiles. When E2 = H the calculated $\Delta$G value is equal to 0 kJ mol$^{-1}$ due to the species on both sides of the equation being the same. This allows for the electrophiles shown in figure 3.29 to be directly compared to H in affecting the ability of **B** to accept a proton.

|  | **Gibbs Energy (ΔG/kJ mol$^{-1}$)** |  |  |
|---|---|---|---|
| **E2** | **Ru** | **Fe** | **Mg** |
| **H** | 0 | 0 | 0 |
| **F** | 5 | 7 | 10 |
| **$CF_3$** | 68 | 76 | 57 |
| **$CH_3$** | 16 | 21 | 13 |
| **$SiH_3$** | 34 | 43 | 48 |
| **$^t$Bu** | -12 | -14 | -36 |
| **TMS** | 5 | 5 | 5 |

**Table 3.7** Calculated ΔG values for proton transfer between the aromatized and dearomatized complex (Shown in figure 3.29).

As expected, the calculated ΔG values show significant deviation from the value for H (0 kJ mol$^{-1}$) for each electrophile and the same trend is seen in that the $CF_3$ complex is the least favourable and $^t$Bu complex being the most favourable ($CF_3$>$SiH_3$>$CH_3$>F>TMS>$^t$Bu). The high electronegativity of the $CF_3$ group dramatically reduces the ability of the complex to act as a base as the trifluoromethyl group draws electron density away from the carbon centre to which the proton is attached and so a high ΔG value is obtained. However, when the fluorine atoms are substituted for hydrogens to give the more electron donating methyl-substituted complex a significant reduction by approximately -50 kJ mol$^{-1}$ is observed (Ru-$CF_3$ ΔG = +67.91 kJ mol$^{-1}$, Ru-$CH_3$ ΔG = +16.42 kJ mol$^{-1}$) indicating that the ability of the complex to act as a base can be improved through careful selection of the substituent group attached at the methylene carbon. This is further shown when a methyl group is replaced with a tert-butyl group as in doing this the ΔG value further decreases for example ΔG (Fe-$CH_3$) = +20.58 kJ mol$^{-1}$ and in Fe-$^t$Bu the ΔG value is now -13.59 kJ mol$^{-1}$. Table 3.7 also shows that when silicon-based electrophiles are used in place of the corresponding carbon-based groups proton transfer to the dearomatized complex becomes less favourable as for Ru-$CH_3$ ΔG = 16.42 kJ mol$^{-1}$ and Ru-$SiH_3$ ΔG = +33.55

kJ $mol^{-1}$ showing an increase for the silicon-based group. From the data in table 3.7 it can be seen that for all of the metal centres investigated by substituting H for a tert-butyl group in the dearomatized complex proton transfer is more favourable compared with the other electrophiles used as when E2 = *ᵗ*Bu the calculated ∆G value = -12.44 kJ $mol^{-1}$ (Ru), -13.59 kJ $mol^{-1}$ (Fe) and when the nature of the metal centre is changed from a non-transition metal a significantly lower ∆G value is obtained, Mg-$^{t}$Bu ∆G = -36.01 kJ $mol^{-1}$. Despite the results in table 3.7 indicating that by changing the electrophile proton transfer can become more favourable, the reactions still gave a positive ∆G value showing an unfavourable reaction with only the $^{t}$Bu substituted complexes showing a favourable proton transfer. Unfavourable proton transfer is natural in the complexes with electron withdrawing substituents (F, $CF_3$) however weak electron donating groups gave similar results suggesting there is another factor influencing the reactivity at this site.

The influence of the steric bulk around the methylene carbon was investigated to see if this had any effect on the reactivity of the complex, this was done by using the percentage buried volume model which calculates the bulk of a ligand coordinated to the metal centre and this value is given as percentage buried ($V_{\%bur}$). As expected, the complexes in which the more sterically demanding groups ($^{t}$Bu/TMS) have been introduced larger values are obtained however there is little change between each electrophile although differing values can be seen for each metal centre investigated; Mg = 55% - 57.4%, Ru = 67.9%-70.7% and Fe = 72.5% - 75.4%. Given the small change in the sterics of the complex and the large differences between the calculated ∆G values it can be assumed that the steric bulk around the carbon to which the proton attaches has a minimal effect on the ability of the complex to accept a proton at that position. This is reinforced in the steric maps generated as it shows a large steric bulk in the ligand backbone particularly with the $^{t}$Bu and TMS which both gave the most favourable proton transfer.

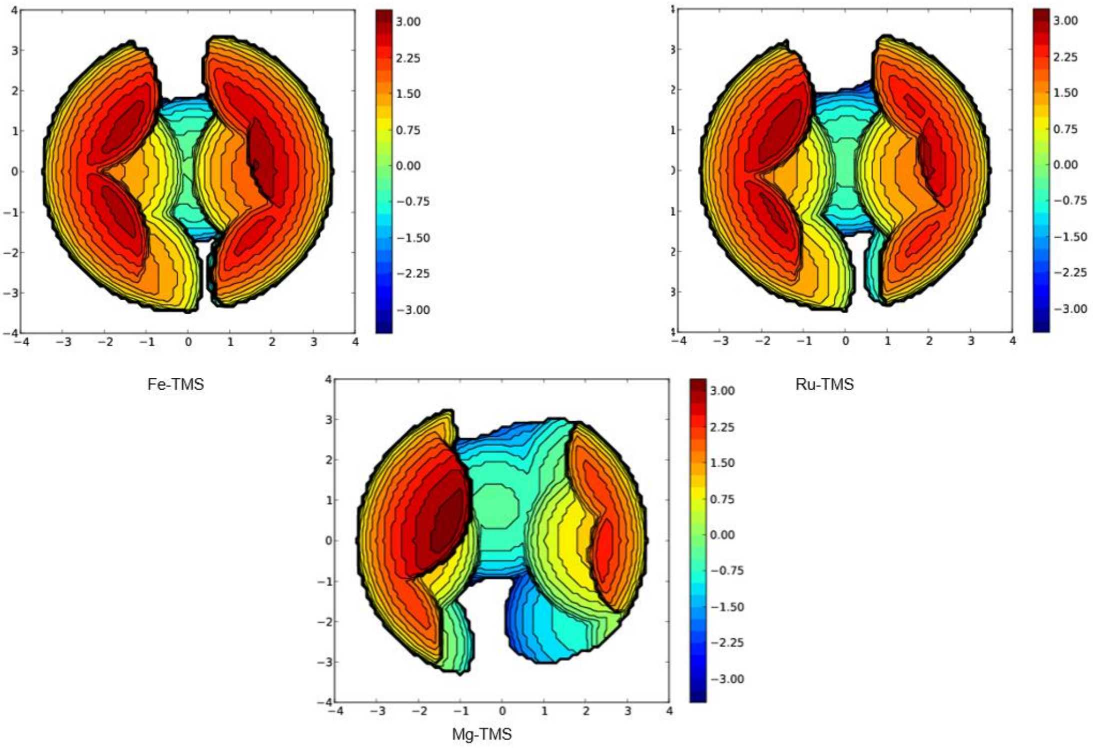

Fe-TMS

Ru-TMS

Mg-TMS

**Figure 3.30** Steric maps for TMS- substituted complexes. The left region depicts the side to which the proton attaches.

The lack of effect of the steric bulk around the methylene carbon is in part due to the ability of the tert-butyl groups and the TMS group to rearrange to allow addition of the proton as shown in the structures above. The effect of this is increased steric bulk around the metal centre could potentially affect the onward reactivity of the complex.

Having investigated the effect changing the group attached to the methylene carbon has on the ability of the complex to accept a proton, altering the metal centre from ruthenium to a first-row transition metal in Iron and then using magnesium (group 2 metal) was investigated to determine what importance the properties of the metal centre has in this reaction. In the previous sections (3.3.1 and 3.3.2) it was shown that by introducing different electrophiles into the ligand backbone only minimal effects were seen at the metal centre. Therefore, it can be assumed that by changing the metal centre little to no change will be observed between the respective $\Delta G$ values and table 3.7 demonstrates this although with some exceptions. For the F, $CH_3$, $SiH_3$ and TMS substituted complexes by altering the metal centre a minimal change is reflected in the calculated $\Delta G$ value for example Ru-$CH_3$ $\Delta G = +16.42$ kJ mol$^{-1}$, Fe-$CH_3$ $\Delta G = +20.58$ kJ mol$^{-1}$ and Mg-$CH_3$ $\Delta G = +13.39$ kJ mol$^{-1}$ which demonstrates that although using magnesium gives a lower $\Delta G$ value the difference with the ruthenium value is only 3 kJ mol$^{-1}$ and 7 kJ mol$^{-1}$ for the iron species. The $^t$Bu and $CF_3$ substituted species however show significant deviation between the metal centres investigated and in both cases proton transfer is more favourable for the magnesium species as Mg-$^t$Bu $\Delta G$ = -36.01 kJ mol$^{-1}$ whereas calculated values of -12.44 kJ mol$^{-1}$ and -13.59 kJ mol$^{-1}$ were obtained for the corresponding ruthenium and iron species respectively.

# 4. Conclusions and Future Work

In conclusion addition of F and $CF_3$ to a pincer ligand backbone was demonstrated, a single product could not be isolated and characterised due to the preferred formation of the reprotonated pincer complex (**4a)**. NMR and ESI-MS confirm addition of the F and $CF_3$ group although the exact position to which the groups are attached cannot be confidently assigned. Reactions with alkylating agents with the dearomatized pincer complex gave no promising results. Future research should focus on optimising the synthesis to favour formation of the electrophile substituted complex over the reprotonated species. Optimisation of this step should involve efforts to further exclude moisture from the reaction. Reactions should be repeated using the alkylating agents described in this thesis however before use these reagents should be dried to reduce moisture content and distilled before use if necessary. This could not be done for this work due to time constraints. Having the ability to synthesise the substituted complexes in good yields will allow for in-depth characterisation and the study of the onward reactivity of the complex.

Computational work carried out showed that adding a substituent group into the ligand backbone has no appreciable effect on the geometry of the metal complex. However, when a non-transition metal is used a significant distortion of the complex is observed. The magnesium complexes showed distortion from the natural geometries and so synthesis of these may prove difficult. It has been demonstrated that by altering the nature of the added electrophile from electron-withdrawing to electron-donating the ability of the complex to act as a base can be significantly improved. The calculations indicate that the tBu and TMS substituted complexes should be used for further reactivity studies and these gave the most favourable reaction. Future research in this area could identify a suitable catalytic reaction and investigate whether the substituted complexes show any catalytic improvements.

# 5. Experimental

## 5.1 General Considerations

All manipulations unless otherwise stated were performed under an $N_2$ environment using standard Schlenk line and glovebox techniques. Hexane, pentane, diethyl ether and methanol were dried using an innovative technologies anhydrous solvent engineering system. Tetrahydrofuran was distilled over sodium (under argon) and then stored over 4Å molecular sieves. $D_2$-dichloromethane was dried by stirring over $CaH_2$ before being vacuum distilled onto 3Å molecular sieves, degassed by three freeze-pump-thaw cycles and stored in the glovebox. $P(^{t}Bu_2)Cl$ was purchased from sigma-aldrich and distilled under reduced pressure before use. All other chemicals were purchased from commercial vendors and used as recieved. $RuHCl(CO)(PPh_3)_3$, $^{tBu}PNP$ and $RuHCl(CO)(^{tBu}PNP)$ were all synthesised by following previously reported procedures. NMR spectra were recorded on a JEOL ECS400 with operating frequencies of 399.78 MHz ($^{1}H$), 161.83 MHz ($^{31}P$) and and 376.17 MHz ($^{19}F$). All chemical shifts are reported in ppm and referenced internally to the residual solvent peak ($d_2$-DCM = 5.32 ppm, $CDCl_3$ = 7.26 ppm). Mass spectra were recorded on a Bruker micrOTOF MS instrument (ESI).

All geometry optimisations were performed at the (RI-) BP86/SVP level of theory followed by frequency calculations at the same level. All calculations were performed using the TURBOMOLE package using the resolution of identity (RI) approximation.[68–74] All structures were visualised using Facio and Jmol.[75,76] $\%V_{bur}$ values were calculated for all complexes using the (RI-) BP86/SVP optimised structures using the SambVca 2.0 package.[77] The sphere radius was set to 3.5Å with bondi radii scaled by 1.17 used and mesh spacing for the integration grid was 0.1Å.

## 5.2 Synthesis of [RuHCl(CO)(PPh$_3$)$_3$]

To a 500ml round bottomed flask was added triphenylphosphine (18.96 g, 72.3 mmol, 6.1 eq.) in 100ml n-propanol. The solution was heated until vigorous reflux then RuCl$_3$.XH$_2$O (2.634 g, 11.9 mmol, 1 eq.) in 20ml n-propanol was added down the condenser. 40 ml formaldehyde was then added immediately after. The educts were washed with 20 ml n-propanol and the solution was left at reflux for 30 minutes. After 30 minutes the reflux was stopped, and the solution was allowed to cool to room temperature. The solution was filtered to isolate the solid product which was subsequently washed alternately with water (4 x 10 ml) and ethanol ( 4 x 10 ml) to yield a grey-brown product. Yield: 9.29 g, 82%.

**$^1$H NMR** (400 MHz, CDCl$_3$): $\delta$ = 6.9-7.8 (m, 93H, Ru-(PPh$_3$)$_3$), -7.2 (d, 1H, Ru-H) ppm.

**$^{31}$P NMR** (400 MHz, CDCl$_3$): $\delta$ = 39.7 (s, 1P)

## 5.3 Synthesis of 2,6-bis((di-tert-butylphosphino)methyl)pyridine ($^{tBu}$PNP)

2,6-lutidene (1.26 ml, 16.23 mmol, 1 eq.) was added to diethyl ether (6 ml) and hexane (3 ml) in a Schlenk flask. The solution was cooled to 0°C and n-BuLi (8.0 ml, 32.46 mmol, 2 eq.), 2.7M in hexanes, was added dropwise and the solution was now deep orange in colour. The solution was heated to 40°C and left to stir for 17 hrs. After this time the solution was cooled to -78°C and di-tert-butylchlorophosphine (4.0 ml, 32.46 mmol, 2 eq.) was added dropwise, a colour change to dark red was observed. The solution was warmed to room temperature and stirred 1 hour. Methanol (15 ml) was then added to quench the solution to yield a pale-yellow solution. The solvents were removed *en vacuo* to yield an off-white residue. The residue was dissolved in methanol (15 ml) and hexane (25 ml). The hexane phase was separated from the methanol phase via cannula. The methanol phase was washed with hexane (10 ml) and the hexane phase was again separated from the methanol phase via cannula. The collected hexane phases were concentrated under reduced pressure to give a white solid. The solid was dissolved in hot diethyl ether (5 ml) and stored in the freezer overnight. The solvent was cannula filtered and the white crystalline solid remaining was dried in *vacuo*. Yield = 1.09 g, 17%.

**$^1$H NMR** (400 MHz, $CD_2Cl_2$): *δ* = 1.09 (d, $^3J_{H,P}$ = 11.04 Hz, 36H, $P^tBu_2$), 2.94 (d, $^2J_{H,P}$ = 3.08 Hz, 4H, PCH), 7.14 (d, $^3J_{H,H}$ = 7.62 Hz, 2H, H3/H5), 7.42 (t, $^3J_{H,H}$ = 7.62 Hz, 1H, H4) ppm.

**$^{31}$P NMR** (400 MHz, $CD_2Cl_2$): *δ* = 36.1 (s) ppm

## 5.4 Synthesis of [RuHCl(CO)($^{tBu}$PNP)]

To an oven dried Schlenk flask was added [RuHCl(CO)($PPh_3$)$_3$] (748 mg, 0.79 mmol, 1 eq.) in 10 ml THF. $^{tBu}$PNP (342 mg, 0.79 mmol, 1 eq.) was dissolved in 20 ml THF and transferred to the complex suspension. The solution was heated to 65°C and stirred for 3 hrs. Over this time the solution turned dark yellow in colour. After 3 hrs the solution was allowed to cool to room temperature and the solvent was removed in *vacuo*. Pentane (40 ml) was added, and the solution was stored in the freezer overnight. The solution was filtered to yield a pale-yellow product. Recrystallisation of the desired product was achieved by using hot THF (10 ml) and rt pentane (30 ml). Yield = 252 mg, 57%

**$^1$H NMR** (400 MHz, $CD_2Cl_2$): *δ* = -15.1 (t, $^2J_{H,P}$ = 19.9 Hz, 1H, RuH), 1.20 (t, $^3J_{H,P}$ = 6.29 Hz, 18H, $P^tBu_{up}$), 1.41 (t, $^3J_{H,P}$ = 6.92 Hz, 18H, $P^tBu_{down}$), 3.34 (dt, $^2J_{H,H}$ = 19.9 Hz, 2H, $PCHH_{up}$), 3.88 (dt, $^2J_{H,H}$ = 19.15 Hz, 2H, $PCH_{down}H$), 7.19 (d, $^3J_{H,H}$ = 7.77 Hz, 2H, $H^3/H^5$), 7.51 (t, $^3J_{H,H}$ = 7.44 Hz, 1H, $H^4$) ppm.

**$^{31}$P{$^1$H} NMR** (400 MHz, $CD_2Cl_2$): 88.8 (d, $^2J_{H,P}$ = 17.07 Hz) ppm.

## 5.5 Synthesis of LiHMDS

To an oven dried Schlenk flask was added HMDS (3.9 ml, 18.6 mmol, 1 eq.) in $Et_2O$ (50 ml). The solution was cooled to 0°C and n-BuLi (9.5 ml,), 2.0 M in hexanes, was added dropwise. The solution was allowed to warm to room temperature and stirred for a further 4.5 hrs. After 4.5 hrs the solvents were removed under reduced pressure to yield a white solid. The solid was washed with ice cold hexane (2 x 20 ml) and dried under vacuum. Yield = 2.04 g, 65.6%.

## 5.6 Fluorination of [RuHCl(CO)($^{tBu}$PNP)

A solution of [RuHCl(CO)($^{tBu}$PNP)] (50 mg, 0.089 mmol) in THF (5 ml) was cooled to -10°C. A cooled solution of LiHMDS (15 mg, 0.089 mmol, 1 eq.) in THF was added to the complex solution and a colour change from yellow to green was observed. At this point a solution of the chosen fluorinating agent (1 eq.) in THF was added and the solution was allowed to stir for 1 hour at room temperature. The solvents were removed in *vacuo* to yield a green residue. A $^{31}$P{$^{1}$H} NMR of this residue was taken in $d_2$-DCM.

## 5.7 Trifluoromethylation of [RuHCl(CO)($^{tBu}$PNP)]

A solution of [RuHCl(CO)($^{tBu}$PNP)] (50 mg, 0.089 mmol) in THF (5 ml) was cooled to -10°C. A cooled solution of LiHMDS (15 mg, 0.089 mmol, 1 eq.) in THF was added to the complex solution and a colour change from yellow to green was observed. At this point a solution of Umemoto’s reagent (36 mg, 0.089 mmol, 1 eq.) in THF (2 ml) was added to the complex solution and the resulting solution allowed to stir for 1 hour at room temperature. The solvents were removed in *vacuo* to yield a green residue which was dissolved in $d_2$-DCM and a $^{31}$P{$^{1}$H} NMR was taken.

## 5.8 Reaction of [RuHCl(CO)($^{tBu}$PNP) with bromoethane

A solution of [RuHCl(CO)($^{tBu}$PNP)] (50 mg, 0.089 mmol) in THF (5 ml) was cooled to -10°C. A cooled solution of LiHMDS (15 mg, 0.089 mmol, 1 eq.) in THF was added to the complex solution and a colour change from yellow to green was observed. At this point bromoethane (48 mg, 0.45 mmol, 5 eq.) and AgOTf (115 mg, 0.45 mmol, 5 eq.) in THF (2 ml) were added to the reaction mixture. The solution was warmed to room temperature and stirred for 1 hour. A portion of the reaction mixture was removed and a $^{31}$P{$^{1}$H} and $^{1}$H NMR taken.

## 5.9 Reaction of [RuHCl(CO)($^{tBu}$PNP)] with TMS-OTf

A solution of [RuHCl(CO)($^{tBu}$PNP)] (50 mg, 0.089 mmol) in THF (5 ml) was cooled to -10°C. A cooled solution of LiHMDS (15 mg, 0.089 mmol, 1 eq.) in THF was added to the complex solution and a colour change from yellow to green was observed. At this point TMS-OTf (40 mg, 0.18 mmol, 2 eq.) and a solution of CsF (27 mg, 0.18 mmol, 2 eq.) in THF (2 ml). The solution was allowed to stir at room temperature for 1 hour. A sample of the reaction mixture was removed and a $^{1}H$ and $^{31}P\{^{1}H\}$ NMR taken.

# 6. Abbreviations

| | |
|---|---|
| Bpy | 2,2’-bipyridine |
| $^{n}$BuLi | n-Butyllithium |
| $^{t}$Bu | tertiary butyl |
| ESI | Electrospray Ionisation |
| FTMP | 1-Fluoro-2,4,6-trimethylpyridinium tetrafluoroborate |
| LiHMDS | Lithium bis(trimethylsilyl)amide |
| MS | Mass Spectrometry |
| NEt$_3$ | Triethylamine |
| NFSI | N-Fluorobenzenesulfonimide |
| NMR | Nuclear Magnetic Resonance |
| OSEF | Outer-Sphere Electrophilic Fluorination |
| Ph | Phenyl |
| ppm | parts per million |
| iPr | Isopropyl |
| Selectfluor | N-Fluoro-N’-methyl-triethylenediamine bis(tetrafluoroborate) |

**NMR Abbreviations**

| | |
|---|---|
| d | doublet |
| dd | doublet of doublets |
| t | triplet |
| dt | doublet of triplets |
| m | multiplet |
| Hz | Hertz |

# 7. References

1 T. Liang, C. N. Neumann and T. Ritter, *Angew. Chemie Int. Ed.*, 2013, **52**, 8214–8264.

2 P. S. Fier and J. F. Hartwig, *J. Am. Chem. Soc.*, 2012, **134**, 10795–10798.

3 A. Casitas, M. Canta, M. Solà, M. Costas and X. Ribas, *J. Am. Chem. Soc.*, 2011, **133**, 19386–19392.

4 D. A. Watson, M. Su, G. Teverovskiy, Y. Zhang, J. Garcia-Fortanet, T. Kinzel and S. L. Buchwaldf, *Science (80-. ).*, 2009, **325**, 1661–1664.

5 M. H. Katcher and A. G. Doyle, *J. Am. Chem. Soc.*, 2010, **132**, 17402–17404.

6 G. Haufe and S. Bruns, *Adv. Synth. Catalyis*, 2002, **344**, 165.

7 K. L. Hull, W. Q. Anani and M. S. Sanford, *J. Am. Chem. Soc.*, 2006, **128**, 7134–7135.

8 M. H. Katcher, A. Sha and A. G. Doyle, *J. Am. Chem. Soc.*, 2011, **133**, 15902–15905.

9 X. Wang, T. S. Mei and J. Q. Yu, *J. Am. Chem. Soc.*, 2009, **131**, 7520–7521.

10 S. J. Lou, D. Q. Xu, A. B. Xia, Y. F. Wang, Y. K. Liu, X. H. Du and Z. Y. Xu, *Chem. Commun.*, 2013, **49**, 6218–6220.

11 S.-J. Lou, D.-Q. Xu and Z.-Y. Xu, *Angew. Chemie Int. Ed.*, 2014, **53**, 10330–10335.

12 Y. Ye and M. S. Sanford, *J. Am. Chem. Soc.*, 2013, **135**, 4648–4651.

13 S. Bloom, C. R. Pitts, D. C. Miller, N. Haselton, M. G. Holl, E. Urheim and T. Lectka, *Angew. Chemie Int. Ed.*, 2012, **51**, 10580–10583.

14 P. S. Fier, J. Luo and J. F. Hartwig, *J. Am. Chem. Soc.*, 2013, **135**, 2552–2559.

15 T. Furuya, H. M. Kaiser and T. Ritter, *Angew. Chemie Int. Ed.*, 2008, **47**,

5993–5996.

16 T. Furuya, A. E. Strom and T. Ritter, *J. Am. Chem. Soc.*, 2009, **131**, 1662–1663.

17 P. Tang and T. Ritter, *Tetrahedron*, 2011, **67**, 4449–4454.

18 H. Park, P. Verma, K. Hong and J.-Q. Yu, *Nat. Chem.*, , DOI:10.1038/s41557-018-0048-1.

19 L. M. Milner, N. E. Pridmore, A. C. Whitwood, J. M. Lynam and J. M. Slattery, *J. Am. Chem. Soc.*, 2015, **137**, 10753–10759.

20 L. M. Hall, D. P. Tew, N. E. Pridmore, A. C. Whitwood, J. M. Lynam and J. M. Slattery, *Angew. Chemie Int. Ed.*, 2017, **56**, 7551–7556.

21 A. Mukherjee and D. Milstein, *ACS Catal.*, 2018, **8**, 11435–11469.

22 C. Gunanathan and D. Milstein, *Chem. Rev.*, 2014, **114**, 12024–12087.

23 T. Zell and D. Milstein, *Acc. Chem. Res.*, 2015, **48**, 1979–1994.

24 J. R. Khusnutdinova and D. Milstein, *Angew. Chemie - Int. Ed.*, 2015, 54, 12236–12273.

25 J. Zhang, M. Gandelman, L. J. W. Shimon, H. Rozenberg and D. Milstein, *Organometallics*, 2004, **23**, 4026–4033.

26 D. Amoroso, A. Jabri, G. P. A. Yap, D. G. Gusev, E. N. Dos Santos and D. E. Fogg, , DOI:10.1021/om040025x.

27 T. Komuro and H. Tobita, , DOI:10.1039/b915395k.

28 D. Hermann, M. Gandelman, H. Rozenberg, L. J. W. Shimon and D. Milstein, *Organometallics*, 2002, **21**, 812–818.

29 Z. Li, T. M. Rayder, L. Luo, J. A. Byers and C. K. Tsung, *J. Am. Chem. Soc.*, 2018, **140**, 8082–8085.

30 J. Zhang, G. Leitus, Y. Ben-David and D. Milstein, *J. Am. Chem. Soc.*, 2005, **127**, 10840–10841.

31 J. Zhang, M. Gandelman, D. Herrman, G. Leitus, L. J. W. Shimon, Y. Ben-

David and D. Milstein, *Inorganica Chim. Acta*, 2006, **359**, 1955–1960.

32 T. Zell and D. Milstein, *Acc. Chem. Res.*, 2015, **48**, 1979–1994.

33 E. Balaraman, B. Gnanaprakasam, L. J. W. Shimon and D. Milstein, *J. Am. Chem. Soc.*, 2010, **132**, 16756–16758.

34 P. Daw, S. Chakraborty, J. A. Garg, Y. Ben-David and D. Milstein, *Angew. Chemie*, 2016, **128**, 14585–14589.

35 M. Gargir, Y. Ben-David, G. Leitus, Y. Diskin-Posner, L. J. W. Shimon and D. Milstein, *Organometallics*, 2012, **31**, 6207–6214.

36 B. Rybtchinski, S. Oevers, M. Montag, A. Vigalok, H. Rozenberg, J. M. L. Martin and D. Milstein, , DOI:10.1021/ja016126t.

37 D. Benito-Garagorri, E. Becker, J. Wiedermann, W. Lackner, M. Pollak, K. Mereiter, J. Kisala and K. Kirchner, *Organometallics*, 2006, **25**, 1900–1913.

38 H. Salem, L. J. W. Shimon, Y. Diskin-Posner, G. Leitus, Y. Ben-David and D. Milstein, *Organometallics*, 2009, **28**, 4791–4806.

39 R. Barrios-Francisco, E. Balaraman, Y. Diskin-Posner, G. Leitus, L. J. W. Shimon and D. Milstein, *Organometallics*, , DOI:10.1021/om400194w.

40 L. P. He, T. Chen, D. X. Xue, M. Eddaoudi and K. W. Huang, *J. Organomet. Chem.*, 2012, 700, 202–206.

41 L.-P. He, T. Chen, D. Gong, Z. Lai and K.-W. Huang, *Organometallics*, 2012, **31**, 5208–5211.

42 W. H. Bernskoetter, S. K. Hanson, S. K. Buzak, Z. Davis, P. S. White, R. Swartz, K. I. Goldberg and M. Brookhart, *J. Am. Chem. Soc.*, 2009, **131**, 8603–8613.

43 S. Kundu, W. W. Brennessel and W. D. Jones, *Inorg. Chem.*, 2011, **50**, 9443–9453.

44 D. Benito-Garagorri, J. Wiedermann, M. Pollak, K. Mereiter and K. Kirchner, *Organometallics*, 2007, **26**, 217–222.

45 M. Mastalir, G. Tomsu, E. Pittenauer, G. Allmaier and K. Kirchner, *Org. Lett.*,

2016, **18**, 3462–3465.

46 A. Vigalok and D. Milstein, *J. Am. Chem. Soc.*, 1997, **119**, 7873–7874.

47 C. M. Jensen, *Chem. Commun.*, 1999, 0, 2443–2449.

48 M. Stradiotto, K. L. Fujdala and T. D. Tilley, *Chem. Commun*, 2001, 1200–1201.

49 Y. Segawa, M. Yamashita and K. Nozaki, *J. Am. Chem. Soc.*, 2009, **131**, 9201–9203.

50 H. Ogawa and M. Yamashita, *Dalt. Trans.*, 2013, **42**, 625–629.

51 E. E. Korshin, G. Leitus, L. J. W. Shimon, L. Konstantinovski and D. Milstein, *Inorg. Chem.*, 2008, **47**, 7177–7189.

52 S. W. Kohl, L. Weiner, L. Schwartsburd, L. Konstantinovski, L. J. W. Shimon, Y. Ben-David, M. A. Iron and D. Milstein, *Science (80-. ).*, 2009, **324**, 74–77.

53 A. Anaby, B. Butschke, Y. Ben-David, L. J. W. Shimon, G. Leitus, M. Feller and D. Milstein, *Organometallics*, 2014, **33**, 3716–3726.

54 E. Khaskin, M. A. Iron, L. J. W. Shimon, J. Zhang and D. Milstein, *J. Am. Chem. Soc.*, 2010, **132**, 8542–8543.

55 R. Langer, Y. Diskin-Posner, G. Leitus, L. J. W. Shimon, Y. Ben-David and D. Milstein, *Angew. Chemie*, 2011, **123**, 10122–10126.

56 R. Langer, G. Leitus, Y. Ben-David and D. Milstein, *Angew. Chemie Int. Ed.*, 2011, **50**, 2120–2124.

57 J. Zhang, E. Balaraman, G. Leitus and D. Milstein, *Organometallics*, 2011, **30**, 5716–5724.

58 A. Mukherjee, A. Nerush, G. Leitus, L. J. W. Shimon, Y. Ben David, N. A. Espinosa Jalapa and D. Milstein, *J. Am. Chem. Soc.*, 2016, **138**, 4298–4301.

59 E. Balaraman, E. Khaskin, G. Leitus and D. Milstein, *Nat. Chem.*, 2013, **5**, 122–125.

60 S. Mazza, R. Scopelliti and X. Hu, *Organometallics*, 2015, **34**, 1538–1545.

61 I. Mellone, N. Gorgas, F. Bertini, M. Peruzzini, K. Kirchner and L. Gonsalvi, *Organometallics*, 2016, **35**, 3344–3349.

62 N. Ahmad, J. J. Levison, S. D. Robinson, M. F. Uttley, E. R. Wonchoba and G. W. Parshall, in *Inorganic Syntheses*, McGraw-Hill Inc., 2007, vol. 15, pp. 45–64.

63 S. G. Frankiss, *J. Phys. Chem.*, 1967, **71**, 3418–3421.

64 L. M. Walter, *Research Report*, 2019.

65 C. Saunders, M. B. Khaled, J. D. Weaver and D. J. Tantillo, , DOI:10.1021/acs.joc.8b00104.

66 R. Langer, M. A. Iron, L. Konstantinovski, Y. Diskin-Posner, G. Leitus, Y. Ben-David and D. Milstein, *Chem. - A Eur. J.*, 2012, **18**, 7196–7209.

67 R. Langer, M. A. Iron, L. Konstantinovski, Y. Diskin-Posner, G. Leitus, Y. Ben-David and D. Milstein, *Chem. - A Eur. J.*, 2012, **18**, 7196–7209.

68 P. Császár and P. Pulay, *J. Mol. Struct.*, 1984, **114**, 31–34.

69 R. Ahlrichs, M. Bär, M. Häser, H. Horn and C. Kölmel, *Chem. Phys. Lett.*, 1989, **162**, 165–169.

70 O. Treutler and R. Ahlrichs, *J. Chem. Phys.*, 1995, **102**, 346–354.

71 K. Eichkorn, O. Treutler, H. Öhm, M. Häser and R. Ahlrichs, *Chem. Phys. Lett.*, 1995, 242, 652–660.

72 K. Eichkorn, F. Weigend, O. Treutler and R. Ahlrichs, *Theor. Chem. Acc.*, 1997, **97**, 119–124.

73 M. Von Arnim and R. Ahlrichs, *J. Chem. Phys.*, 1999, **111**, 9183–9190.

74 P. Deglmann, F. Furche and R. Ahlrichs, *Chem. Phys. Lett.*, 2002, **362**, 511–518.

75 M. Suenaga, *J. Comput. Chem. Jpn.*, 2005, **4**, 25–32.

76 Jmol: an open-source Java viewer for chemical structures in 3D, http://jmol.sourceforge.net/, (accessed 7 October 2020).

77 L. Falivene, R. Credendino, A. Poater, A. Petta, L. Serra, R. Oliva, V. Scarano and L. Cavallo, *Organometallics*, 2016, **35**, 2286–2293.